Frequency-Domain Super-Resolution With Reconstruction Using Compressed Representation (FDSR-RCR) Algorithm for Remote Sensing Satellite Images

Jiaqing Miao, Xiaobing Zhou, Guibing Li, Gaoping Li, Li Zeng, Xiaoguang Liu, and Ying Tan

***Abstract*— In remote sensing image processing for Earth and environmental applications, super-resolution (SR) is a crucial technique for enhancing the resolution of low-resolution (LR) images. In this study, we proposed a novel algorithm of frequency-domain super-resolution with reconstruction from compressed representation. The algorithm follows a multistep procedure: first, an LR image in the space domain is transformed to the frequency domain using a Fourier transform. The frequency-domain representation is then expanded to the desired size (number of pixels) of a high-resolution (HR) image. This expanded frequency-domain image is subsequently inverse Fourier transformed back to the spatial domain, yielding an initial HR image. A final HR image is then reconstructed from the initial HR image using a low-rank regularization model that incorporates a nonlocal smoothed rank function (SRF). We evaluated the performance of the new algorithm by comparing the reconstructed HR images with those generated by several commonly used SR algorithms, including: 1) bicubic interpolation; 2) sparse representation; 3) adaptive sparse domain selection and adaptive regularization; 4) fuzzy-rule-based (FRB) algorithm; 5) SR convolutional neural networks (SRCNNs); 6) fast SR convolutional neural networks (FSRCNNs); 7) practical degradation model for deep blind image SR; 8) the frequency separation for real-world SR (FSSR); and 9) the enhanced SR generative adversarial networks (ESRGANs). The algorithms were tested on Landsat-8 and Moderate Resolution Imaging Spectroradiometer (MODIS) multiresolution images over various locations, as well as on images with artificially added noise to assess the robustness of each algorithm. Results show that: 1) the proposed new algorithm outperforms the others in terms of the peak signal-to-noise ratio, structure similarity, and root-mean-square error and 2) it effectively suppresses noise during HR reconstruction from noisy low-resolution (LR) images, overcoming a key limitation of existing SR methods.**

***Index Terms*— Compressed representation, frequency domain, low-rank regularization model, remote sensing images, smoothed rank function (SRF), super-resolution (SR).**

I. INTRODUCTION

SUPER-RESOLUTION (SR) is an image enhancement technique that constructs higher spatial resolution images—or sequences—from observed low-resolution (LR) images. High-resolution (HR) images can be obtained either by improving the imaging system itself (hardware upgrades) or by developing advanced image-processing techniques after the images have been captured with existing imaging systems. SR techniques for HR image reconstruction are a key research area in remote sensing image processing, as spatially enhanced images allow interpreters to identify finer details and extract more information than from the original LR images. The physical basis for this enhancement lies in the fact that the reconstructed HR image can incorporate information from multiple sources, rather than relying solely on the LR image. For instance, when multiple images of the same scene are acquired nearly simultaneously by imaging systems with varying resolutions and unaligned pixels, the complementary information across these images can be utilized to reconstruct a higher-resolution image than any of the individual constitutive images.

With the advancement of satellite constellations, such as the Geostationary Operational Environmental Satellites constellation (GOES-16–GOES 19 [1], [2], SARAH [3], Sentinel satellites (Sentinel-3 and Sentinel-5 Precursors [4], etc.) [5], multiple images of the same scene taken within short time intervals (e.g., one day to one week) have become common. Furthermore, HR remote sensing image can also be reconstructed from the limited data of a single LR image based on single-frame SR technique [6], [7].

Received 7 February 2025; revised 23 March 2025; accepted 27 March 2025. Date of publication 1 April 2025; date of current version 15 April 2025. This work was supported in part by the National Natural Science Foundation under Grant 12271083, in part by the Science and Technology Project in Sichuan under Grant 2024YFFK0362 and Grant 2024ZYD0087, in part by Sichuan Provincial Program of Traditional Chinese Medicine of China under Grant 2024ZD014, and in part by the Southwest Minzu University Research Startup Funds under Grant RQD2021066. The work of Jiaqing Miao was supported by China Scholarship Council. The work of Xiaobing Zhou was supported by the Established Program to Stimulate Competitive Research (EPSCoR) Program of the National Science Foundation under Grant 2242802. *(Corresponding author: Xiaobing Zhou.)*

Jiaqing Miao, Gaoping Li, Li Zeng, and Xiaoguang Liu are with the School of Mathematics, Southwest Minzu University, Chengdu 610054, China (e-mail: mjq_011114117@163.com).

Xiaobing Zhou is with the Geological Engineering Department, Montana Technological University, Butte, MT 59701 USA (e-mail: xzhou@mtech.edu).

Guibing Li is with the Key Laboratory of Computer Systems, State Ethnic Affairs Commission, College of Computer Science and Artificial Intelligence, Southwest Minzu University, Chengdu 610041, China, and also with the School of Electrical Engineering, Southwest Jiaotong University, Chengdu 611756, China (e-mail: lgb527@swun.edu.cn).

Ying Tan is with the School of Mathematics, Southwest Minzu University, Chengdu 610054, China, and also with the Key Laboratory of Computer System, State Ethnic Affairs Commission, College of Computer Science and Artificial Intelligence, Southwest Minzu University, Chengdu 610041, China (e-mail: ty7499@swun.edu.cn).

Digital Object Identifier 10.1109/TGRS.2025.3556733

1558-0644 © 2025 IEEE. All rights reserved, including rights for text and data mining, and training of artificial intelligence and similar technologies. Personal use is permitted, but republication/redistribution requires IEEE permission.
See https://www.ieee.org/publications/rights/index.html for more information.
Authorized licensed use limited to: Southwest Minzu University. Downloaded on April 18,2025 at 01:24:17 UTC from IEEE Xplore. Restrictions apply.

TABLE I

IMAGES AND REGIONS USED FOR SR IMAGE RECONSTRUCTION

Image Locations and Date			
Antarctic Peninsula	Antarctic Kunlun Station	Flathead lake, Montana	Brazilian rainforest
Date	Date	Date	Date
03/06/2018	03/28/2018	06/25/2017	08/06/2017

However, during the processes of imaging, digitization, data transmission, and storage, various types of noise, such as readout noise during the digitization of charge-coupled device signals, can be introduced. This noise directly affects image quality. In practical applications like target detection [8], traffic and safety monitoring [9], and pattern recognition [10], HR remote sensing images are crucial. While HR images can be acquired through expensive hardware improvement, LR images captured by existing instruments can be enhanced using SR technology, a crucial branch of image processing. In recent years, significant research has focused on SR techniques and their application to reconstruct HR remote sensing images, leading to numerous proposed SR algorithms [11], [12], [13], [14], [15], [16], [17], [18], [19]. For example, Dong et al. [20] developed the adaptive sparse domain selection and adaptive regularization (ASDS-AR-NL) algorithm. Purkait et al. [21] introduced the fuzzy-rule-based (FRB) algorithm for single-band image reconstruction. Zhang et al. [22] proposed a sparse representation-based SR method for image reconstruction. Dong et al. [23] developed an SR convolutional neural network (SRCNN), which was later improved by redesigning the convolutional neural network (CNN) architecture without sacrificing restoration quality fast super-resolution CNN (FSRCNN) [24]. Zhang et al. [25] designed the Practical Degradation Model for Deep Blind Image SR generative adversarial network (BSRGAN), which generates blur effects using convolution approximation with isotropic and anisotropic Gaussian nuclei, adds Gaussian noise of varying levels, and applies Joint Photographic Experts Group (JPEG) compression with different quality factors. This model enhances the feasibility of practical single-image SR applications. Fritsche et al. [26] proposed the frequency separation for the real-world SR (FSSR) model, which improves performance on real-world images by natural image features and separating the image spectrum into low- and high-frequency components during training. Wang et al. [27] explored the enhanced sr generative adversarial networks (ESRGANs) model, which improved SRGAN by introducing nonbatch normalized residual-in-residual-dense blocks and enhancing perception loss, leading to more realistic and natural texture recovery. Liu et al. [28] proposed the spectral–spatial attention-based U-Net to fuse hyperspectral and multispectral images, effectively enhancing both spectral and spatial information through attention modules. Dian et al. [29] developed CNN-Fus, a fusion method based on subspace representation and CNN denoiser for grayscale denoising, which improves HR-hyperspectral image recovery accuracy. Li et al. [30] designed a spectral SR framework by learning a cross-scale relationship and achieved a satisfactory result. Recently, they transferred the spectral unmixing into the SR and hence proposed an effective couple unmixing framework [31]. Deng et al. [32] proposed a novel pyramid Shuffle-and-Reshuffle Transformer (PSRT) for the task of multispectral and hyperspectral image fusion. Extensive experiments on four datasets demonstrate the superiority of the proposed PSRT. Li et al. [33] proposed an enhanced unmixing-inspired unsupervised network with attention-embedded degradation learning to realize multispectral-aided HS-SR. Extensive experimental results on four datasets demonstrate the effectiveness of the proposed methods. Li et al. [34], [35] enhanced the deep image prior for the hyperspectral SR, which can obtain a high-quality reconstruction result.

Despite the progress made in SR algorithms, few studies have focused on SR techniques based on the frequency domain. The SR theory in the frequency domain is relatively simple, with low computational complexity, and is well-suited for parallel computing. However, SR algorithms based on the frequency domain often produce suboptimal results when reconstructing a noisy image. To address this deficiency, we proposed a novel SR reconstruction algorithm. In this new method, a smoothed rank function (SRF) combined with an expanded frequency-domain image is used. Reconstruction is performed on downsampled images in the frequency domain. Instead of using a traditional low-rank function [36], [37], [38], we apply a nonconvex nonlocal SRF. The procedure of the proposed SR algorithm consists of four steps: 1) an LR image is Fourier transformed to the frequency domain; 2) the frequency-domain image is expanded to the desired size (number of pixels) of the HR image; 3) the expanded frequency-domain image is then inverse Fourier-transformed back to the spatial domain to form an initial HR image; and 4) a final HR image is reconstructed from the initial HR image using a low-rank regularization model that incorporates a nonlocal SRF.

II. DATA SOURCES

Two different sets of remote sensing images, namely the Landsat-8 and moderate resolution imaging spectroradiometer (MODIS) datasets, were selected for this study. Table I summarizes the locations and dates on which the images were acquired. The first dataset consists of Landsat-8 L1TP product images from the panchromatic band (503–676 nm) with a spatial resolution of 15 m. These Landsat images were ordered for four different locations: the Antarctic Peninsula, the Chinese Kunlun Station in Antarctica, Flathead Lake in Montana, USA, and rain forests in Brazil.

The second dataset used in this study comprises MODIS images. MODIS data products MOD09GQ and MOD09GA

Authorized licensed use limited to: Southwest Minzu University. Downloaded on April 18,2025 at 01:24:17 UTC from IEEE Xplore. Restrictions apply.

were ordered from the United States Geological Survey's (USGS) data portal: https://earthexplorer.usgs.gov/. The MOD09GQ product is the MODIS Terra Surface Reflectance Daily L2G Global 250 m data, which provides daily surface reflectivity for bands 1 (620–670 nm) and 2 (841–876 nm) at 250-m spatial resolution and 16 bits radiometric range. The MOD09GA product is the MODIS Terra Surface Reflectance Daily L2G Global 500 m and 1 km data, which includes daily surface reflectance for MODIS bands 1–7 at 500-m spatial resolution. The spectral bands of the MOD09GA product include 620–670 nm (B1), 841–876 nm (B2), 459–479 nm (B3), 545–565 nm (B4), 1230–1250 nm (B5), 1628–1652 nm (B6), and 2105–2155 nm (B7). Notably, the first two bands of both the MOD09GQ (250 m) and MOD09GA (500 m) products are identical but differ in spatial resolution. These products are acquired simultaneously, providing an excellent opportunity for evaluating SR algorithms.

III. ALGORITHM DEVELOPMENT

The new SR algorithm for HR image reconstruction is based on a nonconvex, nonlocal regularization model. The development process involves several key steps.

1) *Block-Grouping Method:* A block-grouping approach is introduced to transform a sparse optimization problem into a rank-minimization problem, using self-similarity among image patches [39], [40], [41]. This method is based on the assumption that there are enough images of the same scene exhibiting self-similarity, which is typically the case with remote sensing images of the Earth's surface. A patch-based approach is then used to select image patches with strong correlation to form a matrix with low rank. We used $\hat{x}_{i_j} \in \mathbb{C}^N$ to denote the ith patch at position j. For each sample patch x_i, patches are grouped using the K-nearest neighbors algorithm in local windows (e.g., 50 × 50 window) as shown below [42]:

$$P_i = \left\{ i_j \middle| \left\| x_i - \hat{x}_{i_j} \right\| < C \right\} \tag{1}$$

where C is a constant and P_i is the position of the patch $\hat{x}_{i_j}$. We select m most similar patches, including the sample patch x_i, to form a matrix $X_i = \left[x_{i_0}, x_{i_1}, \ldots, x_{i_{m-1}} \right]$, $X_i \in \mathbb{C}^{n \times m}$.

2) *Matrix Grouping for Similarity:* Since satellite remote sensing images are typically too large for direct singular value decomposition (SVD) [43], [44], the patches are regrouped based on similarity between matrices. This is represented as

$$G_i = \left\{ (i,j) \middle| \left\| X_i - X_j \right\| < C_1 \right\} \tag{2}$$

where C_1 is a constant for similarity matrices, G_i represents the locations of all matrices X_j that are similar to the sample matrix X_i. If matrices satisfy the similarity condition, they are merged; otherwise, they remain separate. Therefore, we get a matrix $Y_i = \left[x_i, x_{i_1}, \ldots, x_{i_t}, x_j, x_{j_1}, \ldots, x_{j_{m-t-2}} \right]$ with two sample patches x_i and x_j, $Y_i \in \mathbb{C}^{n \times m}$. These patches have similar structures and Y_i represents a matrix with low rank.

3) *Noise Suppression and Matrix Decomposition:* To secure low-rankness, noise suppression is crucial. This is achieved by decomposing the matrix Y_i into a form of $Y_i = Z_i + W_i$, where W_i denotes a noise matrix and Z_i represents a low-rank matrix that is obtained as follows:

$$\begin{aligned} Z_i &= \arg\min_{Z_i} \operatorname{rank}(Z_i) \\ &\quad \text{s.t.} \quad \|Y_i - Z_i\|_F^2 \le \sigma_w^2 \end{aligned} \tag{3}$$

where $\|\cdot\|_F^2$ denotes the Frobenius norm and σ_w^2 represents the noise variance. To obtain an approximate solution to (3), the minimization problem is transformed into a nondeterministic polynomial hard problem, using a nonconvex model with an SRF [45]. The SRF is used as an approximation to solve the low-rank minimization problem. The SRF can be represented by

$$G_\delta(Z) = \ell - \sum_{j=1}^{\ell} e^{-\sigma_j^2(Z)/2\delta^2} \tag{4}$$

where Z is a low-rank matrix, $\ell = \min\{n, m\}$, δ is a parameter, and $\sigma_j(Z)$ is the jth singular value of Z. To avoid falling into a local minimum and ensure convergence when solving the minimization function (5), the initial value of δ is set to a large value, and it gradually decreases as iterations proceed. The optimization problem can be expressed as

$$Z_i = \arg\min_{Z_i} \frac{1}{2}\|Y_i - Z_i\|_F^2 + \lambda G_\delta(Z_i) \tag{5}$$

where λ is a regularization parameter.

A. Model Convergence Analysis

To establish an SR algorithm for HR reconstruction of remote sensing images using the Alternating Direction Method of Multipliers (ADMMs) method [46], the SRF function $G_\delta(Z)$ as shown in (4), is a pseudo-norm function. We assume $Q(Z) = P(\sigma(Z))$, where $\sigma(Z)$ represents the SV of the matrix Z. We also assume Z has the SVD form $Z = U\Sigma V^T$, where U and V are orthogonal matrices, $\Sigma = \operatorname{diag}\left(\sigma_1, \sigma_2, \ldots, \sigma_{n_1}\right)$ is a diagonal matrix of singular values, $n_1 = \min\{n, m\}$. The derivative of $Q(Z)$ with respect to Z is given by [22]

$$\nabla Q(Z) = \frac{\partial Q(Z)}{\partial Z} = U \operatorname{diag}(\theta) V^T \tag{6}$$

where $\theta = (\partial P(Z)/\partial Z)$ is the derivative of P with respect to $\sigma(Z)$. The derivative of the function $H_\delta(Z) = \sum_{j=1}^{\ell} e^{-\sigma_j^2(Z)/2\delta^2}$ with respect to Z is given by

$$\begin{aligned} &\frac{\partial H_\delta(Z)}{\partial Z} = \\ &\quad U \operatorname{diag}\left(-\frac{\sigma_1}{\delta^2} e^{-\sigma_1^2/2\delta^2}, -\frac{\sigma_2}{\delta^2} e^{-\sigma_2^2/2\delta^2}, \ldots, -\frac{\sigma_\ell}{\delta^2} e^{-\sigma_\ell^2/2\delta^2} \right) V^T. \end{aligned} \tag{7}$$

For $Z \in \mathbb{C}^{n \times m}$, the minimization problem is solved by applying weighted thresholds to the singular values, as shown below:

$$Z = \arg\min_{Z} \frac{1}{2}\|Y - Z\|_F^2 + \lambda G_\delta(Z). \tag{8}$$

Authorized licensed use limited to: Southwest Minzu University. Downloaded on April 18,2025 at 01:24:17 UTC from IEEE Xplore. Restrictions apply.

Proof: The minimization of the function

$$K(Z) = (1/2)\|Y - Z\|_F^2 + \lambda G_\delta(Z)$$

can be expressed in a gradient form as follows:

$$\begin{aligned}\nabla K(Z) = \frac{\partial K(Z)}{\partial Z} &= (Z - Y)\\ &+ \lambda U \operatorname{diag}\left(\frac{\sigma_1}{\delta^2} e^{-\sigma_1^2/2\delta^2}, \frac{\sigma_2}{\delta^2} e^{-\sigma_2^2/2\delta^2}, \dots, \frac{\sigma_\ell}{\delta^2} e^{-\sigma_\ell^2/2\delta^2}\right) V^T\\ &= 0. \end{aligned} \tag{9}$$

To solve (12) for Z, the gradient descent method is used. The iterative form for Z is

$$Z^{(k+1)} = Z^{(k)} - \alpha \nabla K(Z) \tag{10}$$

where α represents the step size.

B. Establishment and Solution With Respect to the Model

Using the SRF as the low-rank regularization term, the SR reconstruction model for HR images is formulated as

$$\begin{aligned} x &= \Phi^{-1}(U\Phi\omega)\\ \left(\hat{x}, \hat{Z}_i\right) &= \underset{\hat{x}, \hat{Z}_i}{\arg\min} \|y - \mathrm{DFx}\|_2^2\\ &\quad + \eta \sum_i \left\{\|R_i x - Z_i\|_F^2 + \lambda G_\delta(Z_i)\right\},\\ (\Phi x)_\Omega &= (\Phi\omega)_\Omega \end{aligned} \tag{11}$$

where ω is the LR image and U and Φ are the up-sized and Fourier-transformed matrices, respectively. The matrix $y \in \mathbb{C}^M$ is a compression vector from an HR remote sensing image that is resized in the frequency domain. $x \in \mathbb{C}^N$ represents the reconstructed SR image, and the matrices $D \in \mathbb{C}^{M \times N}$ and F correspond to down-sized and Fourier-transformed matrices. The regularization parameters η and λ are applied to enforce sparsity. $R_i\ x \doteq \left[R_i x, R_{i_1} x, \dots, R_{i_t} x, R_j x, R_{j_1} x, \dots, R_{j_{n-t-2}} x\right]$ represents a patch group at positions $(i, i_1, \dots, i_t, j, j_1, \dots, j_{n-t-2})$ and generates a matrix whose columns are similar to x_i. Z_i is a low-rank matrix. $G_\delta(Z_i)$ is the SRF function. $(\cdot)_\Omega$ denotes the projection function that holds the entries of $\Phi\omega$ in Ω while making others to be zeros. Therefore, the matrix becomes low-rank. The method can now be used to reconstruct HR images.

We use the ADMM method [47], [48] and Split Bregman [49] methods to solve (11). First, we decompose the problem into two subproblems.

Subproblem 1:

$$\hat{Z}_i = \underset{\hat{Z}_i}{\arg\min} \|R_i x - Z_i\|_F^2 + \lambda G_\delta(Z_i). \tag{12}$$

Subproblem 2:

$$\hat{x} = \underset{\hat{x}}{\arg\min} \|y - DFx\|_2^2 + \eta \sum_i \|R_i x - Z_i\|_F^2. \tag{13}$$

For the Subproblem 1, we solve it directly using $Z_i = U diag\left(\sigma_1, \sigma_2, \dots, \sigma_{n_1}\right) V^T$. The step size α should be gradually reduced for better results. Based on trial and error, we set the step size as $\alpha = \delta^2$. For Subproblem 2, we solve it using ADMM that leads to the augmented Lagrangian function

$$\begin{aligned}(x, z, \mu) = \underset{x}{\arg\min} &\|y - FDx\|_2^2\\ &+ \beta\left\|x - z + \frac{\rho}{2\beta}\right\|_2^2 + \eta \sum_i \|R_i z - Z_i\|_F^2 \end{aligned} \tag{14}$$

where $\rho \in \mathbb{C}^N$ denotes the Lagrangian multiplier and $\beta > 0$ and $\eta > 0$ are the regularization parameters. $z \in \mathbb{C}^N$ is an auxiliary variable. The iterative process for solving the augmented Lagrangian is expressed as

$$\begin{cases} z^{(k+1)} = \underset{z}{\arg\min} \beta^{(k)} \left\|x^{(k)} - z^{(k)} + \frac{\rho^{(k)}}{2\beta^{(k)}}\right\|_2^2\\ \qquad\qquad + \eta \sum_i \left\|R_i z^{(k)} - Z_i\right\|_F^2;\\ x^{(k+1)} = \underset{x}{\arg\min} \left\|y - DFx^{(k)}\right\|_2^2\\ \qquad\qquad + \beta^{(k)} \left\|x^{(k)} - z^{(k+1)} + \frac{\rho^{(k)}}{2\beta^{(k)}}\right\|_2^2;\\ \rho^{(k+1)} = \rho^{(k)} + \beta^{(k)}\left(x^{(k+1)} - z^{(k+1)}\right);\\ \beta^{(k+1)} = \gamma \beta^{(k)} \end{cases} \tag{15}$$

where $\gamma > 1$ denotes a constant. The solution converges and can be expressed as

$$\begin{aligned} &z^{(k+1)} =\\ &(\eta \sum_i R_i^T R_i + \beta^{(k)} I)^{-1} (\beta^{(k)} x^{(k)} + \frac{\mu^{(k)}}{2} + \eta \sum_i R_i Z_i) \end{aligned} \tag{16}$$

where $\sum_i R_i^T R_i$ is a diagonal matrix. The average is expressed as $\sum_i R_i Z_i$. Hence, we have

$$\begin{aligned} &x^{(k+1)} =\\ &F^H\{(D^T D + \beta^{(k)})^{-1} (D^T y + F(\beta^{(k)} z^{(k+1)} - \frac{\rho^{(k)}}{2}))\}. \end{aligned} \tag{17}$$

Using the ADMM method, we update both the matrix Z_i and the SR image x. The pseudocode of a specific algorithm is shown in Algorithm 1. The SR model is called the frequency-domain super-resolution with reconstruction using compressed representation (FDSR-RCR) algorithm.

IV. RESULTS AND ANALYSIS

To assess the performance of the newly developed model, we applied the model to a Landsat image and a MODIS image. An LR image was first synthesized by resizing a Landsat-8 panchromatic image, originally consisting of 1000 × 1000 pixels, with a scale of 0.25, to an LR image with 250 × 250 pixels. The LR image was resampled from the original image using the cubic interpolation method, resulting in a synthetic LR image with a resolution of 60 m. For the MODIS images, the MOD09GA (500 m resolution) was resized with scales of 0.5 and 0.25 to generate LR images of 400 × 400 and 200 × 200 pixels, respectively, from the original MOD09GA images at a 1-km resolution, which consists of 800 × 800 pixels cross two bands. These synthetic LR MODIS images were then used to reconstruct HR MODIS images. The reconstructed HR MODIS images, which have 250-m resolution, were compared with the original MOD09GQ data, also at 250-m resolution, acquired at the same time as the

Authorized licensed use limited to: Southwest Minzu University. Downloaded on April 18,2025 at 01:24:17 UTC from IEEE Xplore. Restrictions apply.

Algorithm 1 Pseudocode of the FDSR-RCR Algorithm

```
Step 1. Expanded Fourier transform
    First, transform an LR image into an image in the Fourier domain; second, expand the frequency-domain image to an HR image of the desired size; third, apply the inverse Fourier transform to obtain the initial HR image.
Step 2. Initialization:
    Initialize the image $x$ using the inverse Fourier transform; then set parameters and initialize the weights as described in [45]; and lastly, for each sample patch $x_i$, form the patch group $P_i$ and find the corresponding position $G_i$.
Step 3. Main Loop
    Establish patch data sets $Y_i$ and transform patches into vectors.
Step 4. Solve the Subproblems
For Subproblem 1:
    Let the collection be $Z_i^{(0)} = Y_i$;
Inner loop: (Eq.(12))
For $j = 1, 2, \ldots, J$
        (I) the SVD of the low-rank matrix $Z_i$ is calculated by using $Z_i = U diag(\sigma_1, \sigma_2, \ldots, \sigma_{n_1}) V^T$;
        (II) calculate the gradient $\nabla Q(Z_i^{(j-1)})$ of $Q(Z_i^{(j-1)})$ with respect to $Z_i^{(j-1)}$ according to Eq.(7);
        (III) If $j = J$, then $Z_i = Z_i^{(j)}$.
End for.
For Subproblem 2:
For $l = 1, 2, \ldots, L$
Inner loop: (solving Eq.(13))
For $k = 1, 2, \ldots, K$
        (I) $z^{(k+1)}$ is calculated by using Eq.(16);
        (II) $x^{(k+1)}$ is calculated by using Eq.(17);
        (III) update $\rho$ and $\beta$:
        $\rho^{(k+1)} = \rho^{(k)} + \beta^{(k)}(x^{(k+1)} - z^{(k+1)})$,
        $\beta^{(k+1)} = \gamma\beta^{(k)}$;
        (IV) If $k = K$, then $x^{(l)} = x^{(k+1)}$.
End for
If $l = L$, then the final reconstructed HR image $\hat{x} = x^{(l)}$ is obtained.
End for
            $(\Phi x)_\Omega = (\Phi\omega)_\Omega$.
End
```

MOD09GA data. The noise of different levels was then added to the LR images to create synthetic noisy LR images. Below, we demonstrate how HR images were reconstructed from the LR images with synthetic noise using the SR algorithm developed to test the robustness of the algorithm. A block diagram illustrating the entire workflow is shown in Fig. 1.

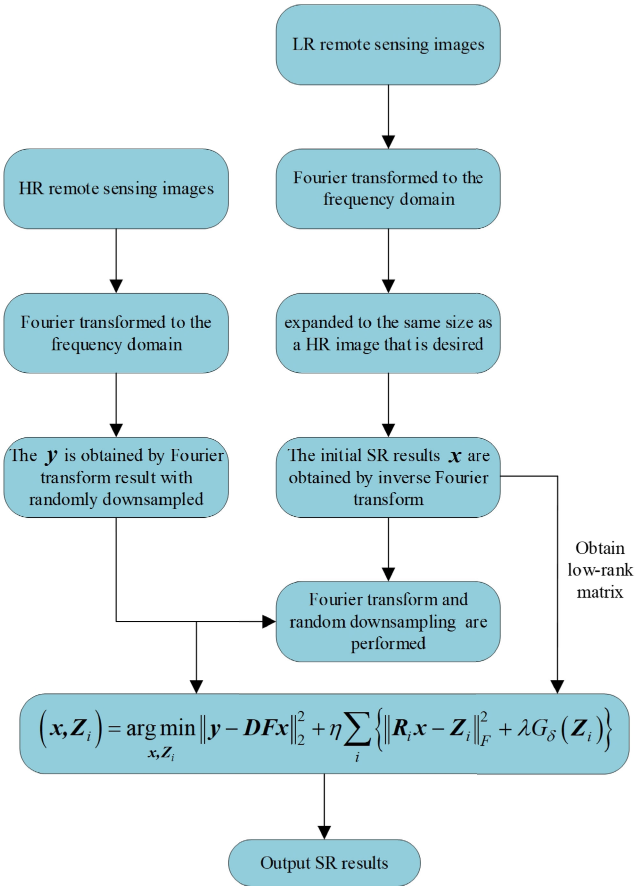

Fig. 1. Block diagram for the entire workflow.

The reconstructed HR images were compared with the original HR image to assess the performance of the new SR algorithm. For the regularization parameters λ and η, when the parameter ranges were set to $\lambda \in (0.3, 0.95)$ and $\eta \in (0.05, 0.25)$, respectively, the FDSR-RCR algorithm did not necessarily achieve the best reconstruction results for the Landsat-8 panchromatic and MODIS images, but it ensured convergence of the algorithm. The values of the parameters λ and η were adjusted for different images. Since the nonconvex function was used as a regularization term, the algorithm is relatively sensitive to a few parameters. Thus, values of the parameters were set within these ranges and fine-tuned to achieve optimal reconstruction results. For the low-rank matrix Z_i, $m = 54$ similar patches were selected for each example patch. After several trials, the patch size was chosen to be 5 × 5. To simplify calculations, three pixels were taken in both left-right and up-down orientations to extract the sample patches from the image tensor. The computation was performed on a Dell Precision 7760 server with 128 GB RAM and an Intel[1] CPU Core[2] i7-11800H @ 2.30 GHz.

Fig. 2(a)–(d) shows the original Landsat-8 panchromatic images over the Chinese Kunlun Station in Antarctica, the Antarctic Peninsula, Flathead Lake of Montana, USA, and the rain forest in Brazil, respectively. Fig. 2(e) and (f) shows the MODIS images of bands 1 and 2 from the MOD09GA (500 m) product, tile h10v04, covering the Northwestern United States, respectively.

To assess the sensitivity of the newly developed FDSR-RCR model to noise levels in LR images during HR image reconstruction, random noise at various levels was added to the original images. The noise had a zero mean and standard deviations (SD) of 16-bit pixel values: 65 535 × (5.9%), 65 535 × (2%), 65 535 × (6.9%), 65 535 × (3.9%), and

---

[1] Registered trademark.
[2] Trademarked.

Authorized licensed use limited to: Southwest Minzu University. Downloaded on April 18,2025 at 01:24:17 UTC from IEEE Xplore. Restrictions apply.

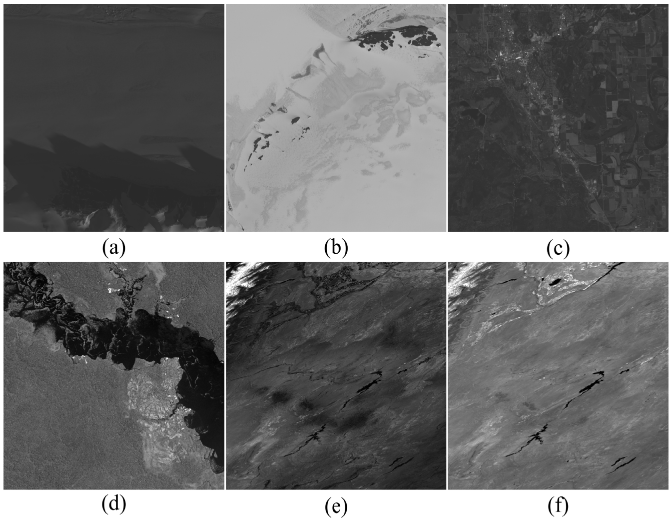

Fig. 2. Original remote sensing images used for algorithm evaluation. (a)–(d) Landsat-8 panchromatic images acquired on June 3, 2018; March 28, 2018; June 25, 2017; June 25, 2017; and August 6, 2017, respectively, covering: (a) Chinese Kunlun Station in Antarctica, (b) Antarctic Peninsula, (c) Flathead Lake, Montana, USA, and (d) Brazilian rain forest. (e) and (f) Images of bands 1 and 2, respectively, from the MODIS MOD09GA (500 m) product (tile h10v04) acquired on June 3, 2018, covering the Northwestern United States.

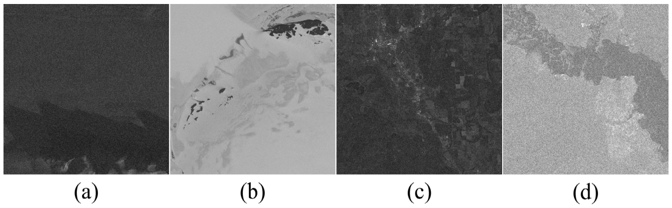

Fig. 3. Synthetic noisy images for algorithm assessment. Images (a)–(d) created by adding random noise with a zero mean and SDs of 65 535 × (5.9%), 65 535 × (2%), 65 535 × (6.9%), and 65 535 × (3.9%), respectively, to the resized LR Landsat-8 images from the original Landsat 8 panchromatic images shown in Fig. 2(a)–(d).

65 535 × (3.9%), respectively. Fig. 3(a)–(d) shows the synthetic noisy images corresponding to the Landsat-8 images from Fig. 2(a)–(d), respectively.

Fig. 3 displays a series of preliminary HR images reconstructed from the series of images resized from the corresponding original noise-free images showed in Fig. 1. The top row shows the resized LR images, listed in the same order from left to right as in Fig. 1. The scale is 0.25 for the Landsat 8 panchromatic images and 0.5 for the MODIS images. The second row shows the corresponding LR images in the frequency domain after the Fourier transform, with pixels sorted so that those at the center of each image have the highest values. These LR images in the frequency domain were then expanded to the same size as the original images displayed in Fig. 1, with the pixel values of the added pixels (the black squared shell in the images shown in the third row) set to 0. The third row shows the corresponding images from the second row but with expanded pixel sizes matching the HR images shown in Fig. 1. These images represent the preliminary HR images in the frequency domain that require further reconstruction. The fourth row shows the corresponding images in the spatial domain after applying the inverse Fourier transform, representing the preliminary HR images in the space domain that will be further reconstructed using the newly developed SR algorithm.

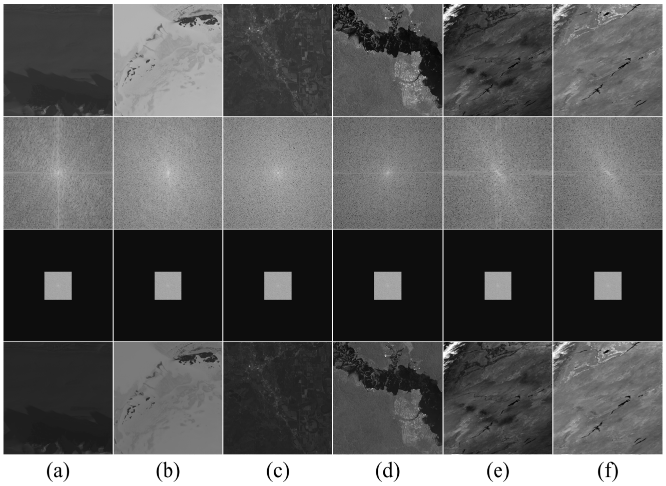

Fig. 4. Top row shows the resized images from the corresponding noise-free images in Fig. 2. The second row shows the corresponding frequency-domain images for the top row. The third row shows the same images in the frequency domain but expanded to the same size as the original images shown in Fig. 2. The fourth row shows the corresponding images in the space domain, obtained by inverse Fourier transform. (a) Kunlun Station in Antarctica. (b) Antarctic Peninsula. (c) Flathead Lake. (d) Rain forest in Brazil. (e) MODIS Band-1. (f) MODIS Band-2.

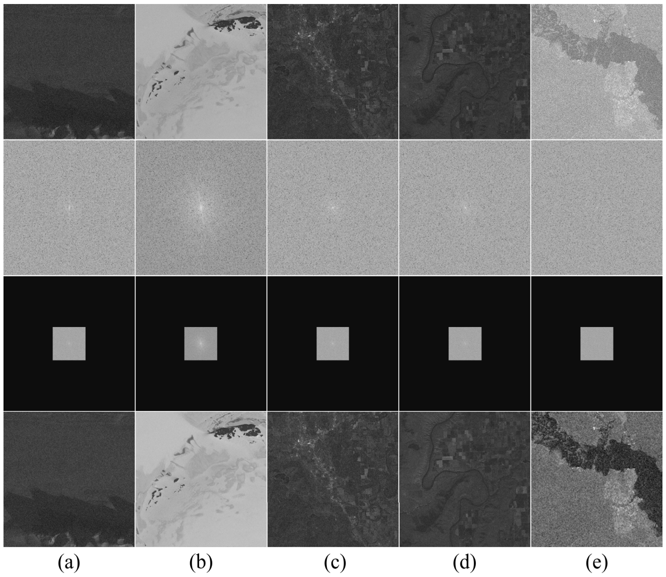

Fig. 5. Images from left to right in the top row are the resized images with a scale of 0.25 from the corresponding noisy images shown in Fig. 3. The second row shows the corresponding images in the frequency domain. The third row shows the corresponding images from the second row, expanded to the same pixel size as the original noisy images shown in Fig. 3. The fourth row shows the corresponding images from the third row in the space domain. (a) Kunlun Station in Antarctica. (b) Antarctic Peninsula. (c) Flathead Lake. (d) Flathead Lake-standby. (e) Rain forest in Brazil.

Fig. 4 displays a series of preliminary HR images reconstructed from the resized images corresponding to the original noise-free images showed in Fig. 2. The top row shows the resized LR images, listed from left to right as in Fig. 2. The second row shows the corresponding LR images in the frequency domain, and the third row shows the

Authorized licensed use limited to: Southwest Minzu University. Downloaded on April 18,2025 at 01:24:17 UTC from IEEE Xplore. Restrictions apply.

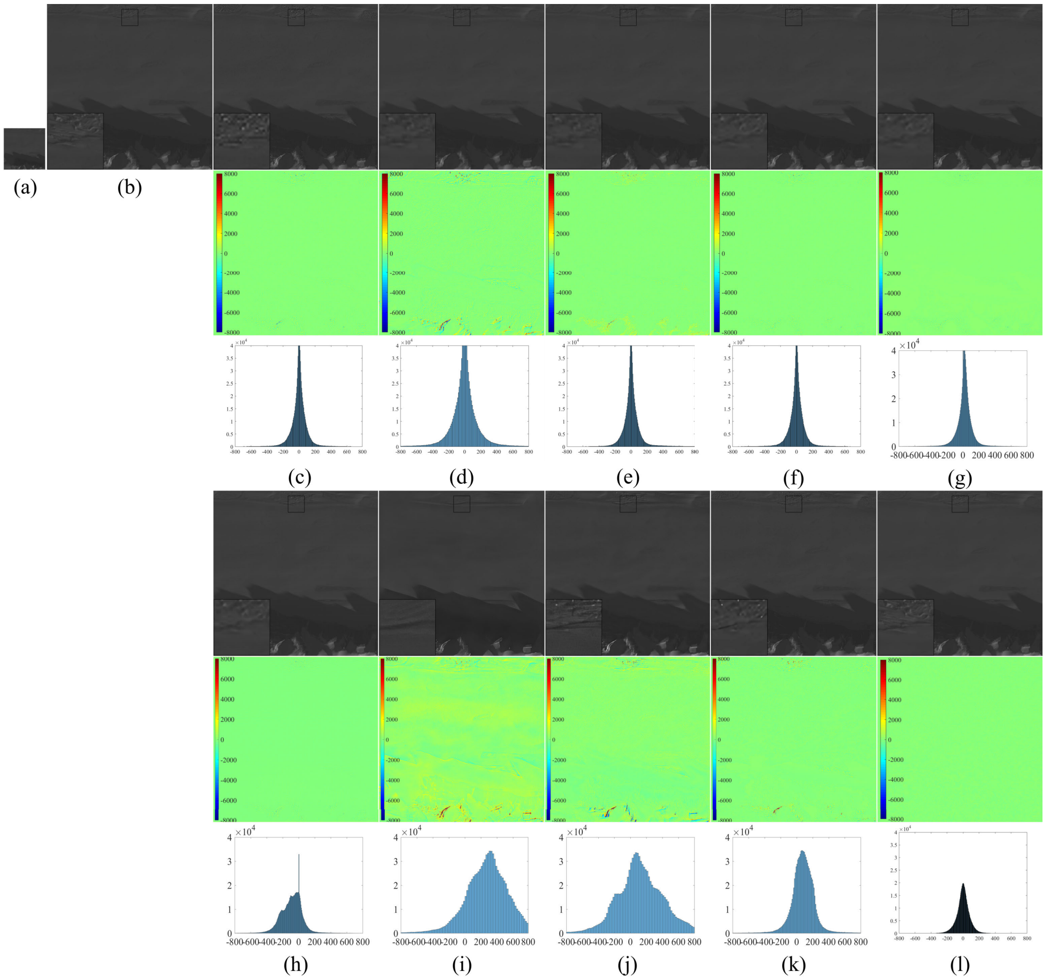

(a) (b) (c) (d) (e) (f) (g) (h) (i) (j) (k) (l)

Fig. 6. (a) Resized Landsat panchromatic image with a scale of 0.25, same as the leftmost image of the top row of Fig. 4. The image covers the Kunlun Station in Antarctica. (b) Original HR Landsat panchromatic image covering the Kunlun Station, Antarctica [same as Fig. 2(a)]. The images of the first and fourth rows are the HR images constructed using (c) bicubic interpolation, (d) sparse representation, (e) ASDS-AR-NL, (f) FRB, (g) SRCNN, (h) FSRCNN, (i) BSRGAN, (j) FSSR, (k) ESRGAN, and (l) FDSR-RCR models, respectively. The images of the second and fifth rows are the difference images between the original HR Landsat panchromatic image and the reconstructed HR image using the corresponding algorithm, respectively. The third and sixth rows are the histograms of the corresponding difference images.

frequency-domain images expanded to match the HR image size. The fourth row shows the corresponding images in the spatial domain after the inverse Fourier transform, representing the initial HR images to be further reconstructed using the newly developed SR algorithm.

Fig. 5 shows a series of the initial HR Landsat-8 images reconstructed from the resized LR images of the synthetic noisy images in Fig. 3. The top row shows the resized LR Landsat-8 images with a scale of 0.25 from the original noisy images. The second row shows the corresponding LR images in the frequency domain, and the third row shows these images expanded to the same size as the HR images. The fourth row shows the corresponding spatial domain images after the inverse Fourier transform, representing the preliminary HR images to be further reconstructed using the newly developed SR algorithm.

A. Numerical Experiments on Noise-Free Remote Sensing Images

The SR images reconstructed from the synthetic noisy images using the FDSR-RCR model were compared with those reconstructed using several existing algorithms: bicubic interpolation, sparse representation, ASDS-AR-NL, FRB, SRCNN, FSRCNN, BSRGAN, FSSR, and ESRGAN. The results are shown in Fig. 6. Fig. 6(c)–(i) displays the reconstructed images using each of the aforementioned algorithms. The corresponding difference images are shown in the second and fifth rows, and histograms of these difference images are in the third and sixth rows.

To enhance the visibility of the details in the difference images (shown in rows 2 and 5 in Fig. 6), histogram equalization was applied. Upon examining the reconstructed images, we found that the FDSR-RCR model preserves sharp edges without noticeable blurring, whereas other SR algorithms exhibit varying degrees of edge blurring. For example, the bicubic interpolation method introduces a slight separation effect, and the FRB, SRCNN, and FSRCNN algorithms cause a noticeable loss of information in the region with dense features or rich texture. The BSRGAN algorithm suffers from uneven lighting, leading to significant reflectivity discrepancies in the target objects, while ESRGAN results in blurring and

Authorized licensed use limited to: Southwest Minzu University. Downloaded on April 18,2025 at 01:24:17 UTC from IEEE Xplore. Restrictions apply.

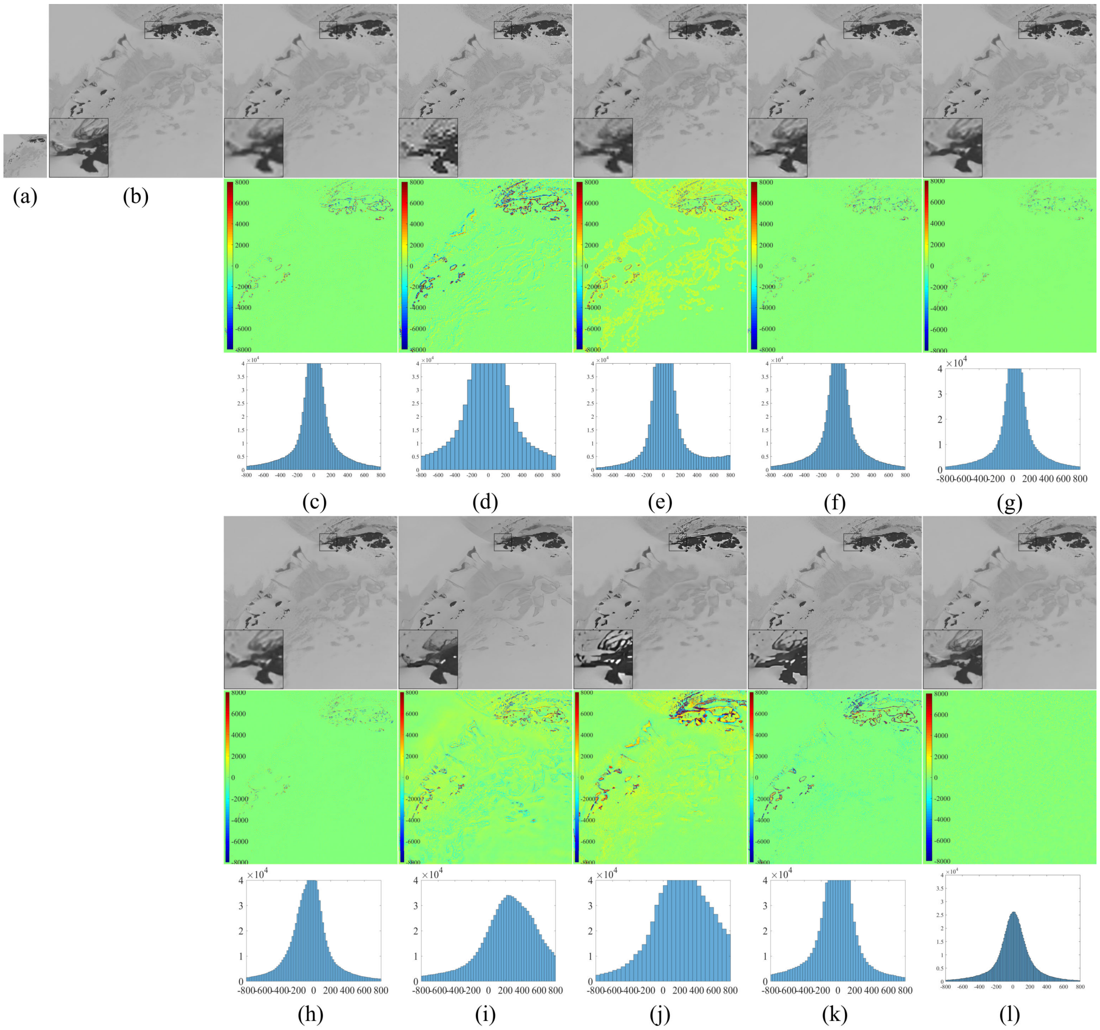

Fig. 7. Same as Fig. 6 but the HR-image reconstruction was performed on the resized Landsat 8 pan-chromatic image covering the Antarctic Peninsula (same as the second-from-the-left image in the top row of Fig. 4).

unclear edges. Images reconstructed using the FSSR algorithm suffer from data loss, leading to partial loss of target objects. In contrast, the FDSR-RCR model effectively suppresses noise during the SR process, retaining more surface details than the other algorithms, as evidenced by the difference images in Fig. 6.

Fig. 7 shows the reconstruction results of the resized Landsat 8 panchromatic image covering the Antarctic Peninsula, using the same algorithms as those in Fig. 6. The sparse representation and ASDS-AR-NL algorithms produce results significantly different from the original HR image, with bicubic interpolation exhibiting obvious edge blurring and loss of details. The sparse representation method also causes a distinct sawtooth effect. The FRB, SRCNN, and FSRCNN algorithms result in data loss in steep areas with many contours, demonstrating the better capacity of the ASDS-AR-NL algorithms in preserving the features in areas of high spatial frequency. The BSRGAN and FSSR algorithms produce uneven lighting, leading to partial loss of target objects and distortion, the ESRGAN algorithm exhibits blurring and significant reflectance differences. Among all, the FDSR-RCR algorithm yields the most accurate and faithful reconstruction.

Fig. 8 presents the reconstructed HR images of the resized Landsat-8 panchromatic image covering the Flathead Lake area using the same algorithms as those in Figs. 6 and 7. For this case, the difference between the HR image reconstructed using sparse representation and the original HR image is the largest. The cubic interpolation and ASDS-AR-NL algorithms show noticeable edge blurring and information loss, especially in regions with complex terrain where the spatial frequency is generally high. The FRB, SRCNN, and FSRCNN algorithms still exhibit data loss and edge blurring. The BSRGAN, FSSR, and ESRGAN suffer from inhomogeneous brightness, with FSSR showing the most pronounced nonuniformity. Reconstruction results of the BSRGAN, FSSR, and ESRGAN algorithms suffer from significant loss of details, with FSSR exhibiting the most severe information loss, maybe due to their smoothing effects. The reconstruction result of the ESRGAN algorithm introduces some details that are not present in the original image, leading to blurred or distorted features of target objects. In the reconstructed images by the FDSR-RCR

Authorized licensed use limited to: Southwest Minzu University. Downloaded on April 18,2025 at 01:24:17 UTC from IEEE Xplore. Restrictions apply.

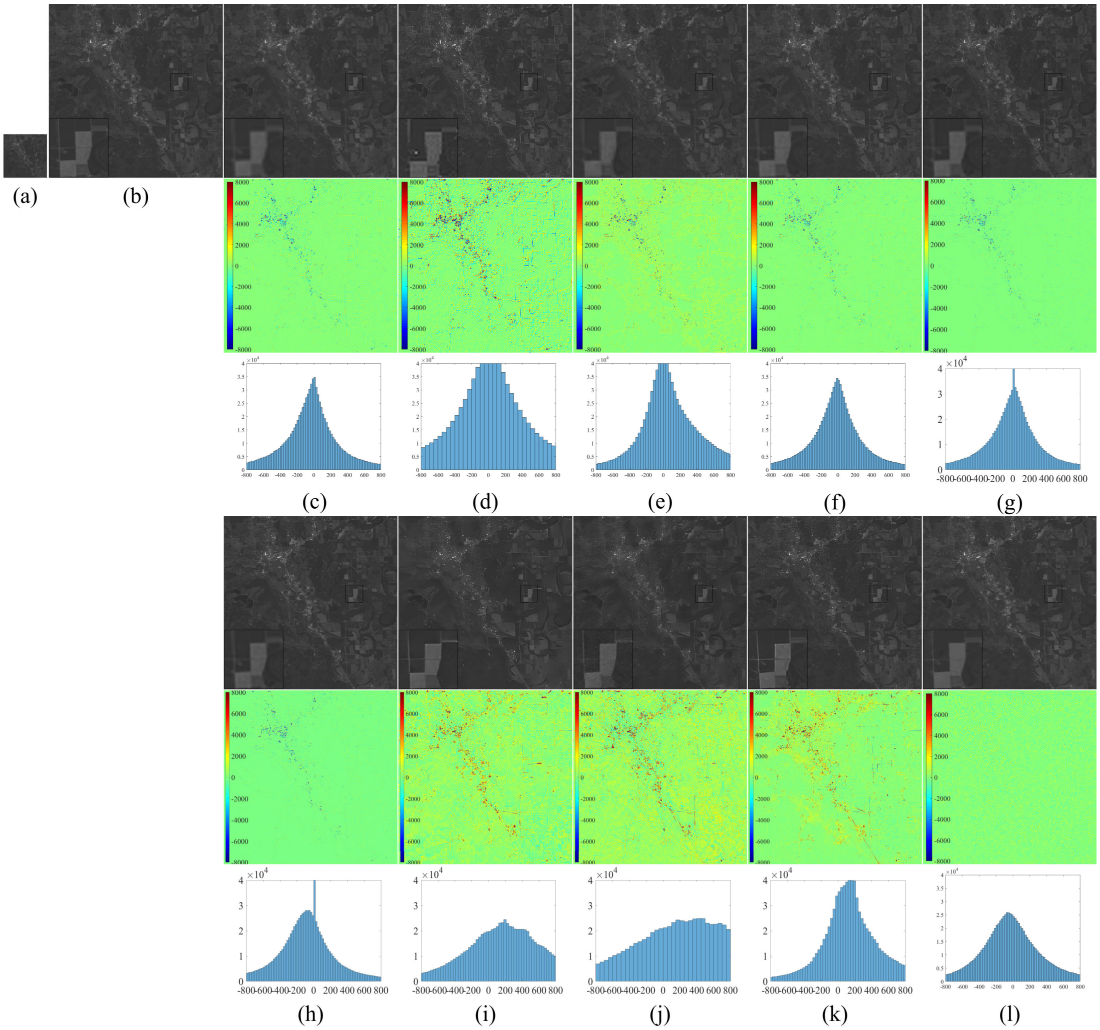

Fig. 8. Same as Fig. 6 but HR-image reconstruction was performed on the resized Landsat 8 panchromatic image covering the Flathead Lake, Montana, USA (same as the third-from-the-left image in the top row of Fig. 4).

algorithm, the partly expanded region (lower left corner) has the best details of boundaries, and features in heterogeneous zones were well preserved.

Fig. 9 shows the reconstructed images for the Brazilian rainforest from the resized Landsat-8 panchromatic image, similar to the results shown in Figs. 6–8. The FDSR-RCR algorithm again outperforms other methods in terms of visual fidelity and feature preservation in forests. The bicubic interpolation and ASDS-AR-NL algorithms display blurred edges, particularly in the enlarged lower-left regions. The sparse representation method introduces a sawtooth effect, while the FRB, SRCNN, and FSRCNN algorithms exhibit strong blurring effects in heterogeneous zones, which are common in forests. The BSRGAN and FSSR algorithms suffer from significant information loss, with BSRGAN being the worst. ESRGAN results in blurred or distorted features, introducing features not present in the original image. The FDSR-RCR algorithm preserves object information, patch boundaries, and feature details effectively, providing the best visual clarity and least distortion in forests, illustrating its superiority in HR image reconstruction for forest investigation.

B. Quantitative Evaluation

The histograms of the difference images shown in the third and sixth rows of Figs. 6–9 are summarized in Table II, which quantifies the number of pixels within a small range around 0 (±520) in each difference image. A higher percentage of pixels within this small range of pixel values around 0 indicates a better reconstruction. Table II shows clearly that the FDSR-RCR algorithm has the largest percentage of pixels concentrated in the narrow range near zero for the images of the Antarctic Kunlun Station (99.97%), Antarctic Peninsula (93.56%), Flathead Lake (90.09%), and Brazilian rainforest (99.99%), indicating that its reconstructed HR images exhibit the highest fidelity to the original Landsat-8 images.

To further quantify the performance of the algorithms, we calculated PSNR, SSIM, and RMSE [50], [51] for the reconstructed images. Results were summarized in Table III. For the Flathead Lake region (Fig. 8), the bicubic interpolation, sparse representation, BSRGAN, and FSSR algorithms have notably higher RMSE values compared to other algorithms. The FDSR-RCR model consistently shows the lowest RMSE. Similarly, for the Kunlun Station, Antarctica (Fig. 6), the

Authorized licensed use limited to: Southwest Minzu University. Downloaded on April 18,2025 at 01:24:17 UTC from IEEE Xplore. Restrictions apply.

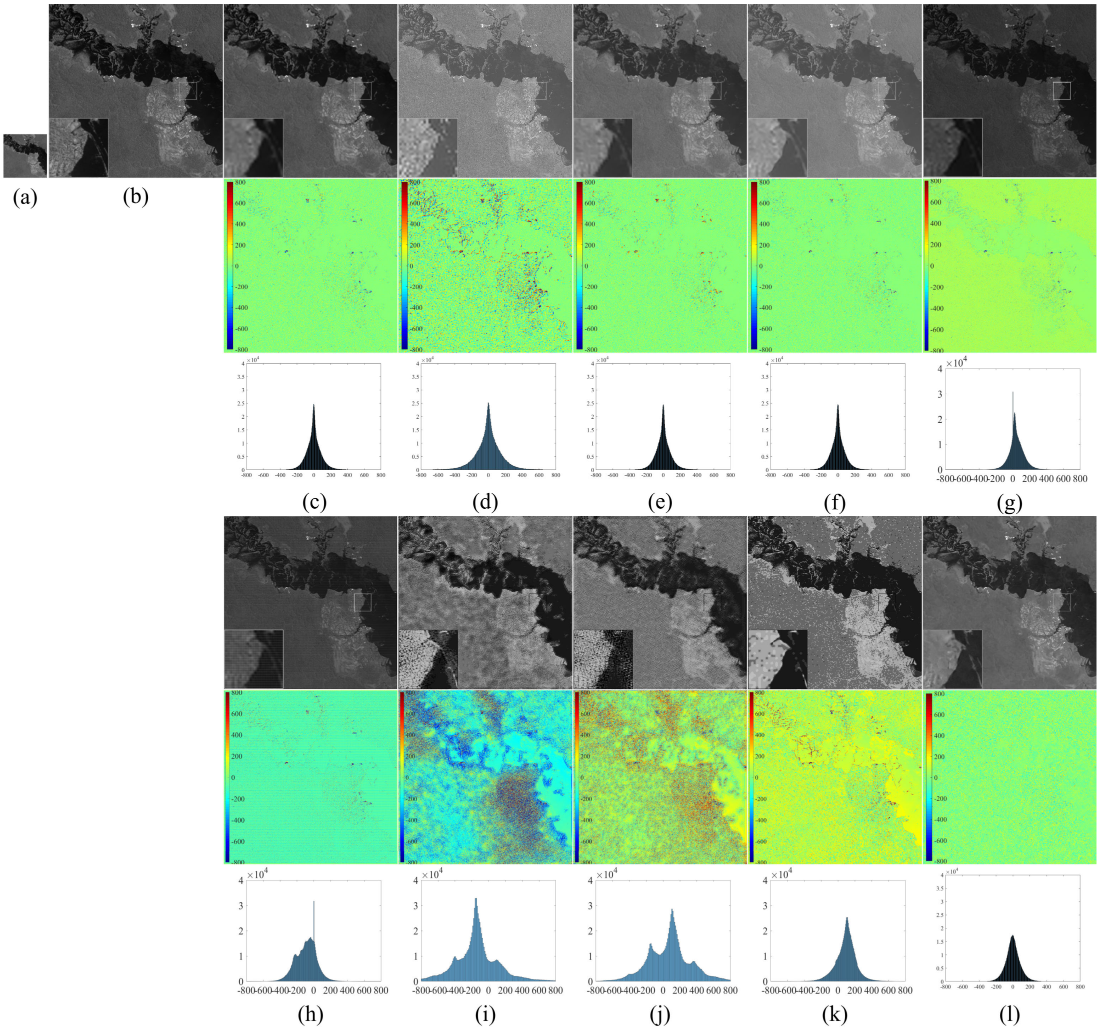

Fig. 9. Same as Fig. 6 but the HR-image reconstruction was performed on the resized Landsat pan-chromatic image covering the rain forest in Brazil (same as the fifth-from-the-left image in the top row of Fig. 4).

TABLE II

Number of Pixels Within a Small Range of Pixel Values Around 0 of the Difference Images Between the Original HR Landsat Panchromatic Image and the Rebuilt HR Images Using Different SR Algorithms

Remote Sensing Images		Antarctic Kunlun Station	Antarctic Peninsula	Flathead Lake	Brazilian rainforest
Difference range of pixel value		[-520,520]	[-520,520]	[-520,520]	[-520,520]
Percentage of pixels occupied	Bicubic	98.22%	88.29%	86.52%	99.93%
	Sparse representation	95.64%	78.39%	71.83%	98.85%
	ASDS-AR-NL	97.71%	75.36%	83.05%	99.88%
	FRB	98.28%	88.80%	87.83%	99.93%
	SRCNN	98.79%	91.72%	80.18%	99.93%
	FSRCNN	98.67%	91.21%	78.95%	99.87%
	BSRGAN	79.45%	66.48%	58.90%	89.82%
	FSSR	87.26%	61.15%	41.48%	93.88%
	ESRGAN	97.49%	85.63%	71.85%	99.51%
	FDE-RCR	99.97%	93.56%	90.09%	99.99%

FDSR-RCR algorithm also maintains the lowest RMSE. For the Brazilian rainforest (Fig. 9), the difference in RMSE values among all algorithms is less pronounced than the Flathead Lake case, but the FDSR-RCR model still achieves the lowest RMSE. The RMSE, PSNR, and SSIM metrics confirm that the FDSR-RCR model outperforms all other algorithms in preserving image quality, with the best visual effects least, and the least errors.

Authorized licensed use limited to: Southwest Minzu University. Downloaded on April 18,2025 at 01:24:17 UTC from IEEE Xplore. Restrictions apply.

TABLE III

VALUES OF RMSE, PSNR, AND SSIM FOR DIFFERENT ALGORITHMS IN GENERATING SR IMAGES FROM THE LANDSAT-8 IMAGES SHOWN IN FIGS. 6–9

Images	Antarctic Kunlun Station			Antarctic Peninsula			Flathead Lake			Brazilian rainforest		
PQIs	RMSE	PSNR	SSIM	RMSE	PSNR	SSIM	RMSE	PSNR	SSIM	RMSE	PSNR	SSIM
Bicubic	171.60	51.64	0.9948	610.66	40.61	0.9696	681.37	39.66	0.9400	93.46	56.92	0.9979
Sparse representation	341.78	45.65	0.9876	1234.41	34.50	0.9341	622.41	40.65	0.9520	162.81	52.10	0.9951
ASDS-AR-NL	195.71	50.50	0.9944	796.20	38.31	0.9597	602.12	40.92	0.9567	96.08	56.68	0.9978
FRB	162.78	52.10	0.9952	546.81	41.57	0.9730	642.85	40.17	0.9458	90.06	57.24	0.9980
SRCNN	154.97	52.52	0.9954	489.24	42.54	0.9757	626.02	40.40	0.9459	100.18	56.31	0.9980
FSRCNN	199.48	50.33	0.9933	499.48	42.36	0.9736	629.78	40.35	0.9453	153.33	52.62	0.9961
BSRGAN	533.09	41.79	0.9829	933.22	36.93	0.9488	1138.00	35.21	0.9021	339.91	45.70	0.9799
FSSR	507.11	42.23	0.9752	1379.93	33.53	0.9255	1369.72	33.60	0.8371	273.40	47.59	0.9842
ESRGAN	275.30	47.53	0.9920	1052.11	35.89	0.9548	1141.43	35.18	0.9141	159.86	52.25	0.9966
FDE-RCR	**83.82**	**57.86**	**0.9986**	**264.13**	**47.89**	**0.9887**	**481.68**	**42.67**	**0.9648**	**87.18**	**57.52**	**0.9983**

C. MODIS Images Reconstruction

For the MODIS images, subimages of 400 × 400 pixels were extracted from Bands 1 and 2 of the MOD09GA (500 m) product. The MOD09GA images were resized by a scale of 0.5 to generate synthetic LR MODIS images with 1-km resolution, which were then used for SR reconstruction. The reconstructed HR images were compared to the original Bands 1 and 2 images from the MOD09GQ product, which have a 250-m resolution.

Figs. 10–13 show the results of SR reconstruction. Figs. 10(a) and (b)–13(a) and (b) show the original MOD09GA and MOD09GQ images, respectively. Figs. 10(c)–(h)–13(c)–(h) display the reconstructed HR images using bicubic interpolation, Sparse Representation, ASDS-AR-NL, FRB, SRCNN, FSRCNN, and FDSR-RCR algorithms, along with the corresponding difference images and their histograms. The FDSR-RCR model consistently provides the best visual effects, with smaller differences from the original images, and better preservation of edges and fine structures compared to the other algorithms.

The last row in Figs. 10–13 shows the histograms of the corresponding difference images. Tables IV and V summarize the number of pixels within a small range (±300) around 0 in the difference images. The FDSR-RCR algorithm again exhibits the highest percentage of pixels within this narrow range, indicating its superior performance in preserving image quality.

In terms of RMSE, PSNR, and SSIM, the FDSR-RCR model outperforms other methods, producing the best reconstructed HR images with superior feature preservation, especially in areas of high spatial frequency. This is further confirmed by the results shown in Tables VI and VII, where the FDSR-RCR model demonstrates the lowest RMSE and the highest PSNR and SSIM values, indicating its superior ability to reconstruct high-quality HR images from LR MODIS data. These results for MODIS images are very similar to the Landsat 8 image, even though the spatial resolution is so different (500 m for MOIS versus 30 m for Landsat 8), indicating the applicability of the FDSR-RCR algorithm to images of a broad range of resolutions.

V. NUMERICAL EXPERIMENTS ON REMOTE SENSING IMAGES WITH SYNTHETIC NOISE

To assess the robustness of the algorithms, evaluation was performed using the Landsat-8 images that cover the Kunlun Station in Antarctica, the Antarctic Peninsula, and the Flathead Lake. The noise of various levels was introduced into the images, as shown in Fig. 3. SR reconstruction was then performed, following a process similar to the noise-free case described in Section IV-A. The reconstruction results produced by the FDSR-RCR model were compared with those from the bicubic interpolation, sparse representation, and FRB algorithms.

The results are presented in Figs. 14–16, and the corresponding values of the perceptual quality index (PQIs) are summarized in Table VIII. Table VIII and Figs. 14–16 show that the FDSR-RCR model maintains a performance comparable to that observed with noise-free images, demonstrating significant advantages in suppressing random noise across different noise levels. The reconstruction results from the FDSR-RCR algorithm are consistently better than those from the other algorithms in terms of visual quality and PQI values. The sparse representation, ASDS-AR-NL, and FRB algorithms also show some capacity for noise suppression, particularly when dealing with images containing lower noise levels, though their performance is not as robust as that of the FDSR-RCR model.

Overall, the FDSR-RCR algorithm stands out with the best PQI values, showing its effectiveness in reconstructing high-quality HR images from noisy input images. This reinforces its strong ability to suppress noise while preserving image details.

VI. DISCUSSION

The success of the SRF regularization method relies heavily on the appropriate adjustment of the weight parameters in

Authorized licensed use limited to: Southwest Minzu University. Downloaded on April 18,2025 at 01:24:17 UTC from IEEE Xplore. Restrictions apply.

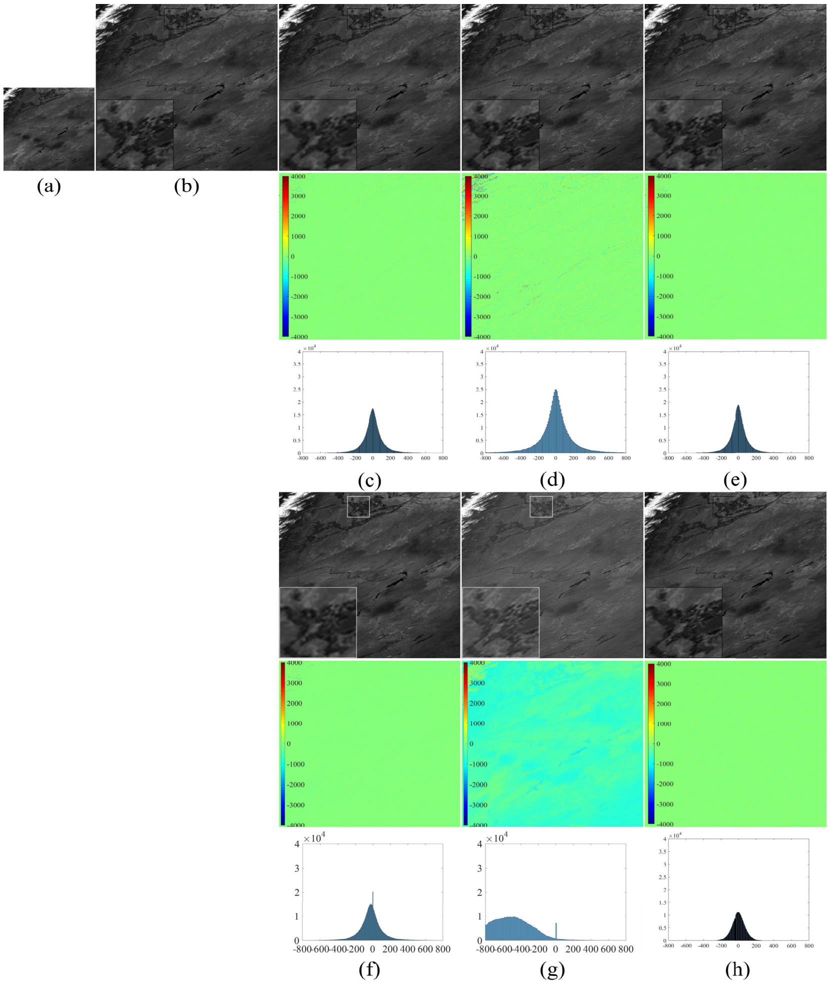

(a) (b) (c) (d) (e) (f) (g) (h)

Fig. 10. Results of SR reconstruction for the MODIS Band-1 image (sur_refl_b01_1) of the MOD09GA product. The image was acquired on June 3, 2018. (a) Original MODIS Band-1 image of the MOD09GA product. (b) Original image of the MODIS Band-1 image of the MOD09GQ product acquired on the same day. (c)–(h) Reconstructed images by the bicubic interpolation, sparse representation, FRB, SRCNN, FSRCNN, and FDSR-RCR models, respectively. (c)–(h) First and fourth rows are the reconstructed HR images using the matching algorithms, the second and fifth rows are the difference images between the original HR image and the matching rebuilt HR images, and the third and sixth rows are the histogram of the difference images for the corresponding algorithm.

TABLE IV

NUMBER OF PIXELS WITHIN A SMALL RANGE OF PIXEL VALUES AROUND 0 OF THE DIFFERENCE IMAGES BETWEEN THE ORIGINAL MODIS IMAGES AND THE REBUILT HR (SCALE OF 0.5) RESULTS USING DIFFERENT SR ALGORITHMS

Remote Sensing Images	Difference range of pixel value	Percentage of pixels occupied			
		Bicubic	Sparse representation	FRB	FDE-RCR
LR MODIS Band-1 (sur_refl_b01_1) image resized with scale of 0.5	[-300,300]	95.71%	88.10%	96.67%	**99.94%**
LR MODIS Band-2 (sur_refl_b01_2) image resized with scale of 0.5	[-300,300]	95.08%	88.32%	96.02%	**99.94%**

the data fidelity and regularization terms. When these weight parameters are optimally selected, this method can produce high-quality HR reconstructions. Experiments were conducted using the Landsat-8 and MODIS images as well as Landsat-8 images with varying levels of added noise. The HR images reconstructed using the bicubic interpolation, sparse representation, ASDS-AR-NL, FRB, SRCNN, FSRCNN, BSRGAN, FSSR, ESRGAN, and FDSR-RCR models were compared to the original HR images. Results consistently show that the newly developed FDSR-RCR algorithm outperforms the other algorithms in fidelity, visual effects, and noise suppression.

Errors typically occur in transition zones between different geological features and land covers where the spatial frequency is generally very high. However, the reconstructed images using the FDSR-RCR method demonstrate that even in these challenging transition zones, the pixel values maintain high

Authorized licensed use limited to: Southwest Minzu University. Downloaded on April 18,2025 at 01:24:17 UTC from IEEE Xplore. Restrictions apply.

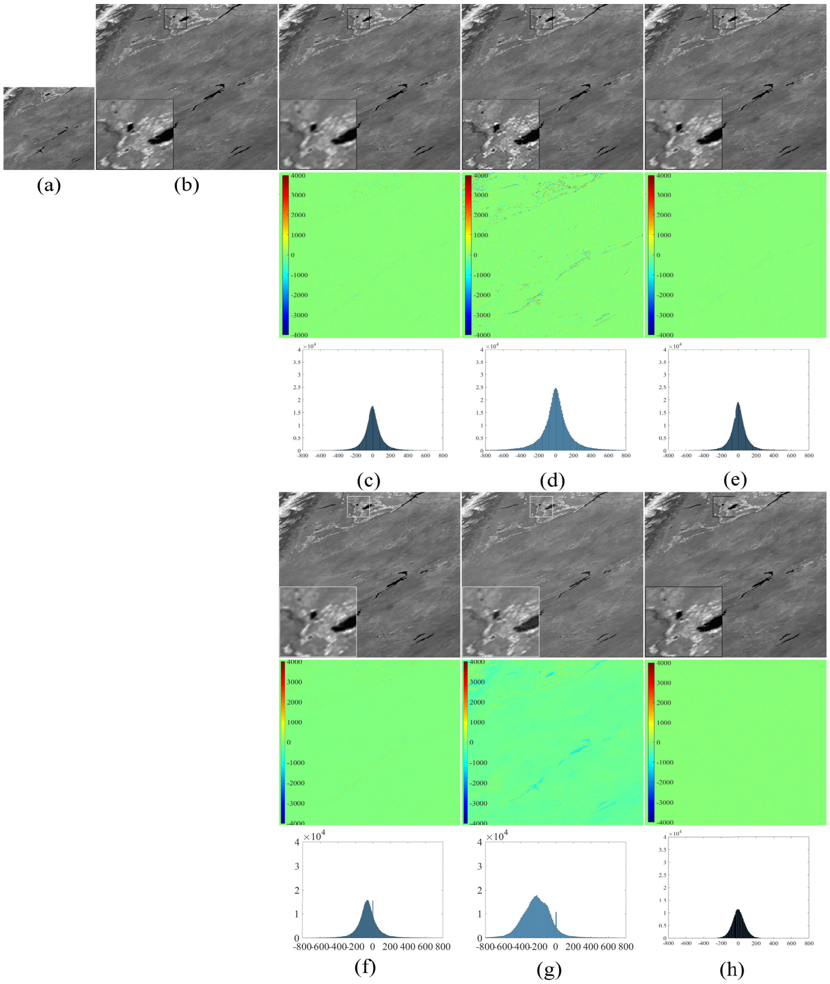

Fig. 11. Same as Fig. 10 but the SR reconstruction was performed on the MODIS Band-2 image (sur_refl_b02_1). The images were acquired on June 3, 2018.

TABLE V

Number of Pixels Within a Small Range of Pixel Values Around 0 of the Difference Images Between the Original MODIS Images and the Rebuilt HR (Scale of 0.25) Results Using Different SR Algorithms

Remote Sensing Images	Difference range of pixel value	Percentage of pixels occupied					
		Bicubic	Sparse representation	FRB	FSSR	ESRGAN	FDE-RCR
LR MODIS Band-1 (sur_refl_b01_1) image resized with scale of 0.25	[-300,300]	90.79%	75.32%	91.67%	75.95%	89.46%	**91.89%**
LR MODIS Band-2 (sur_refl_b02_1) image resized with scale of 0.25	[-300,300]	90.58%	75.72%	91.35%	74.96%	88.51%	**91.92%**

fidelity to the original images. This is critical for remote sensing applications, where reliable delineation of complex geological or ecological surface features is essential. High-fidelity reconstruction in these transition zones is especially important for accurately classifying land cover and land use.

The core objective of SR technology lies in enhancing image resolution and improving detail expression. The algorithm itself does not specify the exact resolution of an image. The study is grounded in the observation that most current optimization-based SR techniques attempt to reconstruct HR images from LR counterparts by solving the nondeterministic polynomial-hard problems. However, such approaches encounter inherent bottlenecks due to the absence of prior information about HR images during reconstruction. To address the limitation, we introduce a novel strategy combining frequency-domain expansion of LR images with random sampling information injection in the frequency domain of HR images. The methodology effectively incorporates prior knowledge of HR images during reconstruction, thereby generating SR images with enhanced details. Com-

Authorized licensed use limited to: Southwest Minzu University. Downloaded on April 18,2025 at 01:24:17 UTC from IEEE Xplore. Restrictions apply.

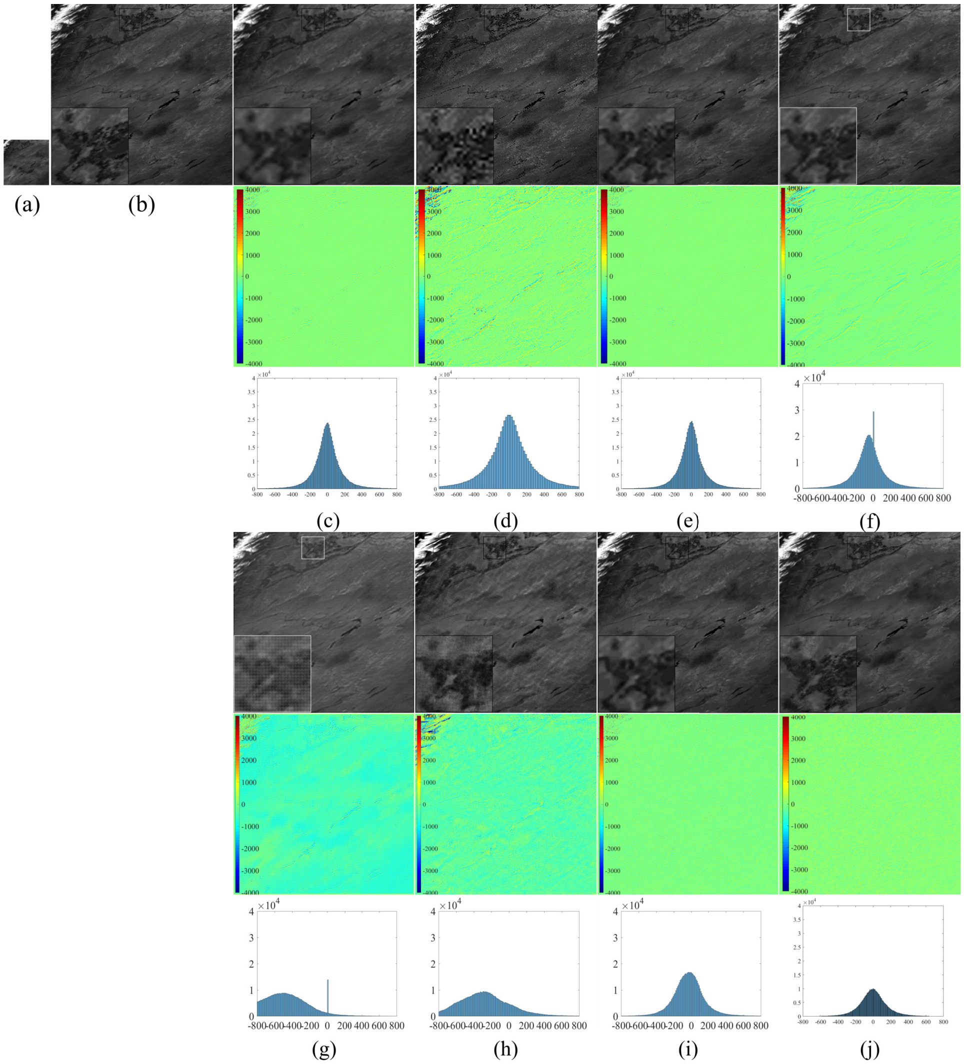

(a) (b)

(c) (d) (e) (f)

(g) (h) (i) (j)

Fig. 12. (a) Resized MODIS Band-1 image of the MOD09GA product with a scale of 0.5. (b) Original image of the MODIS Band-1 image of the MOD09GQ product. (c)–(j) Reconstructed images by the bicubic interpolation, sparse representation, FRB, SRCNN, FSRCNN, FSSR, ESRGAN, and FDSR-RCR models, respectively. (c)–(j) First and fourth rows are the reconstructed HR images using the matching algorithms, the second and fifth rows are the difference images between the original HR image and the corresponding rebuilt HR results, and the third and sixth rows are the histogram of the difference images for the corresponding algorithm.

TABLE VI

VALUES OF RMSE, PSNR, AND SSIM FROM THE SR IMAGE FOR THE CASE STUDIES OF THE MODIS IMAGES SHOWN IN FIGS. 10 AND 11

Images	PQIs	Bicubic	Sparse representation	FRB	FDE-RCR
LR MODIS Band-1 (sur_refl_b01_1) image resized with a scale of 0.5	RMSE	213.05	416.14	203.93	**173.99**
	PSNR	49.76	43.94	50.14	**51.52**
	SSIM	0.9902	0.9686	0.9912	**0.9929**
LR MODIS Band-2 (sur_refl_b01_2) image resized with a scale of 0.5	RMSE	231.35	447.94	218.28	**178.89**
	PSNR	49.04	43.31	49.55	**51.28**
	SSIM	0.9887	0.9681	0.9901	**0.9934**

pared with the original LR images, the reconstructed HR image demonstrates superior spatial resolution and richer textural information, providing enhanced data support for subsequent analytical applications and image interpretation. The algorithm synthetically integrates frequency-domain processing, advanced sampling techniques, and optimization theory. Through systematic operations and constrained processing of LR remote sensing images, it successfully achieves SR images and establishes a robust computational framework for advanced remote sensing image applications. The compre-

Authorized licensed use limited to: Southwest Minzu University. Downloaded on April 18,2025 at 01:24:17 UTC from IEEE Xplore. Restrictions apply.

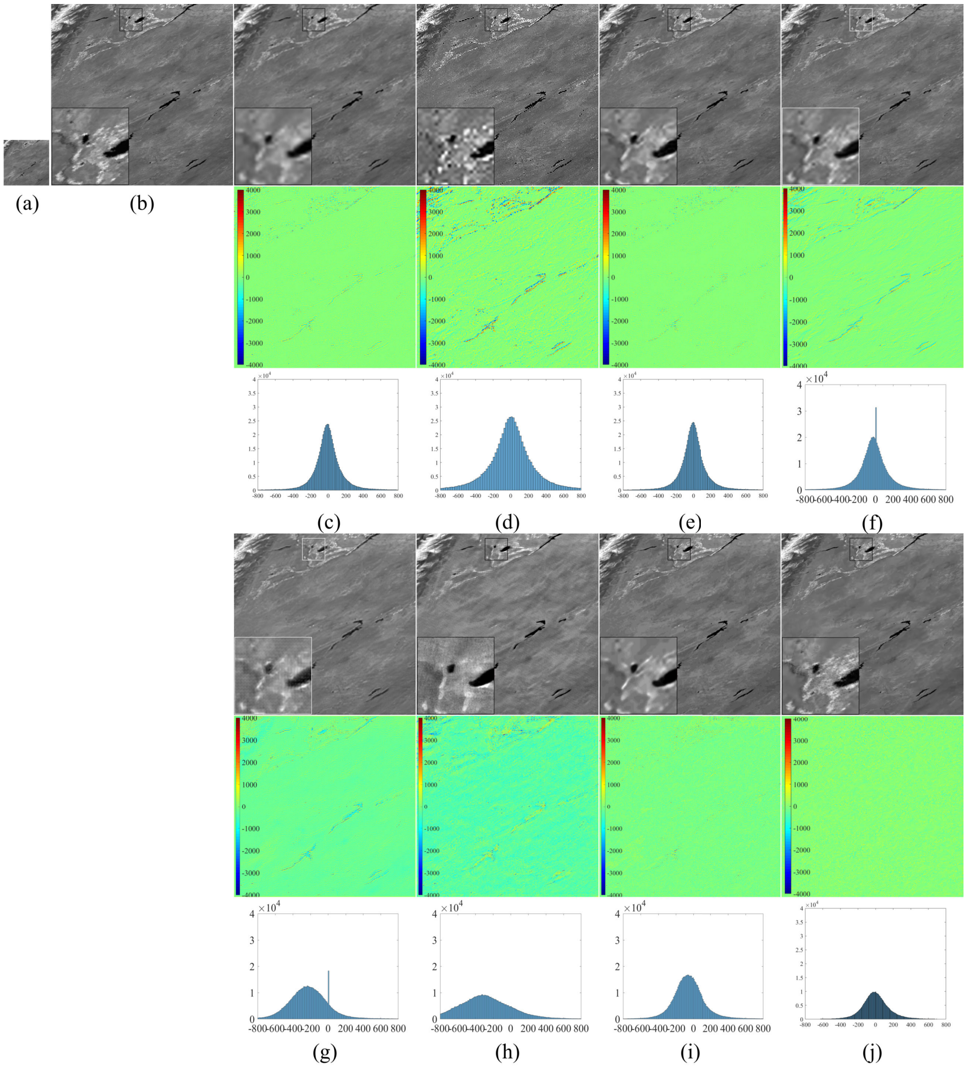

Fig. 13. Same as Fig. 12 but the SR reconstruction was performed on the resized MODIS Band-2 image (sur_refl_b02_1) of the MOD09GA. The image was acquired on June 3, 2018. (a) Resized MODIS Band-2 image with a scale of 0.5, (b) original image of the MODIS Band-1 image, (c) bicubic interpolation, (d) sparse representation, (e) FRB, (f) SRCNN, (g) FSRCNN, (h) FSSR, (i) ESRGAN, and (j) FDSR-RCR models, respectively.

TABLE VII
VALUES OF RMSE, PSNR, AND SSIM FOR THE SR IMAGE FROM THE CASE STUDIES OF THE MODIS IMAGES SHOWN IN FIGS. 12 AND 13

Images	PQIs	Bicubic	Sparse representation	FRB	FSSR	ESRGAN	FDE-RCR
LR MODIS Band-1 (sur_refl_b01_1) image resized with scale of 0.25	RMSE	148.06	256.86	134.55	473.86	217.83	**75.99**
	PSNR	52.92	48.14	53.75	42.82	49.57	**58.71**
	SSIM	0.9952	0.9867	0.9962	0.9596	0.9896	**0.9986**
LR MODIS Band-2 (sur_refl_b02_1) image resized with scale of 0.25	RMSE	157.98	275.89	141.36	466.45	234.10	**74.13**
	PSNR	52.36	47.52	53.32	42.95	48.94	**58.93**
	SSIM	0.9946	0.9852	0.9958	0.9696	0.9890	**0.9987**

hensive approach significantly advances the state-of-the-art in image enhancement by effectively balancing reconstruction accuracy and computational efficiency.

The theoretical performance of the proposed algorithm can be analyzed from two perspectives: computational complexity and reconstruction quality. First, the frequency-domain expansion and inverse Fourier transform convert the spectral information of LR images into the spatial domain to generate an initial HR image. This step achieves a computational complexity of $O(N \cdot \log N)$, where N denotes the total number of pixels in the image. Second, the low-rank regularization model incorporating a nonlocal smooth rank function is employed to optimize the initial HR image through the ADMM iterative optimiza-

Authorized licensed use limited to: Southwest Minzu University. Downloaded on April 18,2025 at 01:24:17 UTC from IEEE Xplore. Restrictions apply.

TABLE VIII

RMSE, PSNR, AND SSIM VALUES FOR DIFFERENT ALGORITHMS IN SR OF THE LANDSAT-8 IMAGES WITH DIFFERENT NOISE LEVELS SHOWN IN FIGS. 14–16

Images	PQIs	Sparse representation	ASDS-AR-NL	FRB	FDE-RCR
Antarctic Kunlun Station	RMSE	1640.94	1071.77	995.14	**112.69**
	PSNR	32.0276	35.73	36.37	**55.29**
	SSIM	0.7267	0.8817	0.8795	**0.9977**
Antarctic Peninsula	RMSE	2024.06	1398.67	638.64	**295.84**
	PSNR	30.21	33.42	40.22	**46.91**
	SSIM	0.7059	0.8579	0.9592	**0.9867**
Flathead Lake	RMSE	2554.50	1334.04	1175.17	**499.38**
	PSNR	28.18	33.83	34.93	**42.36**
	SSIM	0.5630	0.8286	0.8450	**0.9625**

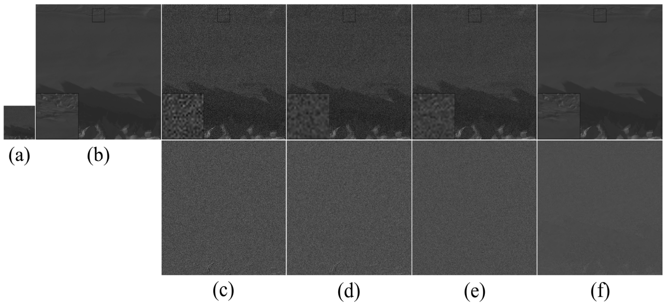

Fig. 14. Results of SR reconstruction from the Landsat-8 images covering the Kunlun Station, Antarctica, with random noise of zero means and an SD of 65 535 × (5.9%). (a) Resized Landsat 8 image with a scale of 0.25. (b) Original Landsat 8 image. (Top row) (c)–(f) Reconstructed HR images by the bicubic interpolation, sparse representation, FRB, and FDSR-RCR models, respectively. (Bottom row) The difference images between the reconstructed HR images and the original images.

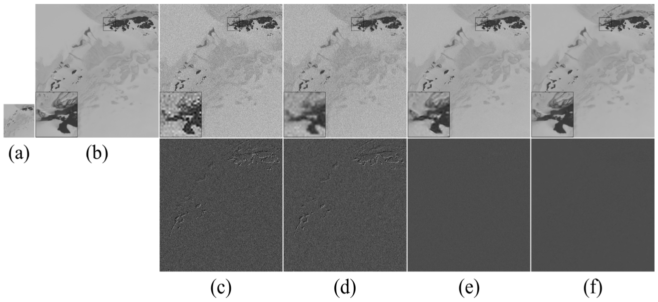

Fig. 15. Same as Fig. 14 but the SR reconstruction was performed on the Landsat-8 image covering the Antarctic Peninsula with the random noise of zero mean and an SD of 65 535 × (2.0%).

tion algorithm, which exhibits a complexity of $O(K \cdot N^2)$, where K represents the number of iterations. The K-nearest neighbors algorithm for identifying similar patches incurs a complexity of $O(m \cdot M)$, where m is the number of pixels per patch in the similarity matrix and M denotes the total number of patches in the image. The computational complexity of performing the SVD scales as $O(\max^3(m, n))$, where n is the number of patches constituting the similarity matrix. Consequently, the overall computational complexity of the algorithm is $O(N \cdot \log N + K \cdot N^2 + m \cdot M + \max^3(m, n))$, which becomes relatively high for large-scale images.

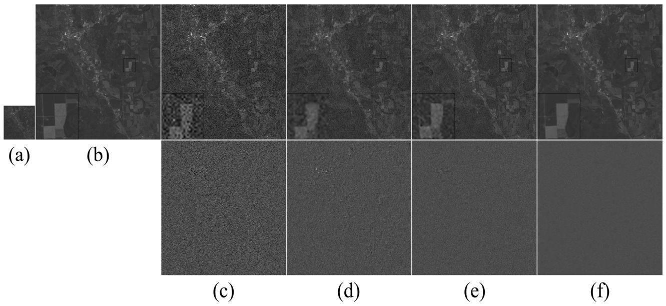

Fig. 16. Same as Fig. 14 but the SR reconstruction was performed on the Landsat-8 image covering the Flathead Lake, Montana, USA, with the random noise of zero means and an SD of 65 535 × (5.9%).

Regarding reconstruction quality, the frequency-to-spatial domain conversion effectively restores global image information. In contrast, the low-rank regularization model enhances reconstruction performance by constraining the image rank and enforcing nonlocal smoothness, which effectively removes noise and enhances details. However, the reconstruction quality depends on factors such as frequency-domain expansion size, regularization parameters, and convergence criteria, necessitating a tradeoff between computational efficiency and reconstruction fidelity.

In summary, the proposed algorithm demonstrates superior performance in image SR tasks and is particularly suitable for applications demanding high-quality reconstruction.

The proposed algorithm also has some limitations: the algorithm performs Fourier transforms and inverse transforms between the frequency and spatial domains, while involving matrix operations in optimizing the objective function. The multiple transformations and complex matrix computations significantly increase the overall computational complexity. Moreover, the incorporation of a computationally intensive nonlocal regularization term for enhanced precision further contributes to the extended execution time. Parameter settings (e.g., regularization parameters η and λ in the objective function) require manual adjustment, demonstrating limited adaptability. Future research will focus on developing an optimized framework utilizing fast transformation techniques to replace conventional Fourier transforms, reducing com-

Authorized licensed use limited to: Southwest Minzu University. Downloaded on April 18,2025 at 01:24:17 UTC from IEEE Xplore. Restrictions apply.

putational overhead in transformation processes. To enhance parameter adaptability, reinforcement learning will be implemented to dynamically adjust parameters in the objective function based on quality feedback from SR outcomes during remote sensing image processing. These proposed improvements aim to mitigate current limitations and enhance the algorithm's practical applicability and reliability in real-world scenarios.

VII. CONCLUSION

In summary, a regularization-based frequency-domain SR algorithm for satellite remote sensing images has been developed, utilizing a nonlocal low-rank SRF function, with reconstruction performed via the ADMM method.

The regularization approach effectively captures inherent structural correlations within the image data, thereby enhancing the reconstruction quality while preserving essential textural details. Simultaneously, the nonlocal nonconvex low-rank regularization method demonstrates exceptional efficacy in exploiting the intrinsic structural redundancy present across similar image patches, thereby establishing itself as a rigorous mathematical framework for HR image reconstruction from LR counterparts. This approach capitalizes on the self-similarity property inherent in remote sensing images, enabling the preservation of fine-scale details while effectively suppressing noise during the reconstruction process. The incorporation of nonconvex regularization further enhances the model's ability to capture complex structural dependencies, resulting in superior fidelity compared to conventional convex regularization methods. The newly developed FDSR-RCR model has been evaluated against various traditional SR algorithms, including bicubic interpolation, sparse representation, ASDS-AR-NL, FRB, SRCNN, FSRCNN, BSRGAN, FSSR, and ESRGAN using Landsat-8 and MODIS images. Results show that the FDSR-RCR model consistently outperforms in terms of better visual quality, lower RMSE, higher PSNR, and SSIM values. This advantage is particularly notable when reconstructing images from LR inputs contaminated by various levels of noise, owing to the model's inherent ability to suppress noise effectively. The FDSR-RCR model demonstrates strong performance in SR reconstruction, even for images with downscaled LR images as small as 0.25 of the original size.

ACKNOWLEDGMENT

The images of the analyzed areas were acquired through the Landsat 8 and MODIS data archive in the United States Geological Survey (USGS) data portal.

REFERENCES

[1] J. Tian, Y. Zhang, K. Knupp, P. Pangle, and J. Comstock, "Summertime continental shallow cumulus cloud detection using GOES-16 satellite and ground-based ceilometer at North Alabama," *J. Geophys. Res., Atmos.*, vol. 129, no. 24, Dec. 2024, Art. no. e2024JD041512.

[2] D. Losos, S. Hoffman, and P. C. Stoy, "GOES-R land surface products at western hemisphere eddy covariance tower locations," *Sci. Data*, vol. 56, no. 1, p. 277, Mar. 2024.

[3] U. Pfeifroth, J. Drücke, S. Kothe, J. Trentmann, M. Schröder, and R. Hollmann, "SARAH-3—Satellite-based climate data records of surface solar radiation," *Earth Syst. Sci. Data*, vol. 16, no. 11, pp. 5243–5265, Nov. 2024.

[4] A. Carbone, R. Restaino, and G. Vivone, "Efficient hyperspectral super-resolution of sentinel-5P data via dynamic multidirectional cascade fine-tuning," *IEEE Geosci. Remote Sens. Lett.*, vol. 21, pp. 1–5, 2024.

[5] P. Reyes-Muñoz et al., "Inferring global terrestrial carbon fluxes from the synergy of sentinel 3 & 5P with Gaussian process hybrid models," *Remote Sens. Environ.*, vol. 305, May 2024, Art. no. 114072.

[6] Y. Xiao, Q. Yuan, K. Jiang, J. He, C.-W. Lin, and L. Zhang, "TTST: A top-k token selective transformer for remote sensing image super-resolution," *IEEE Trans. Image Process.*, vol. 33, pp. 738–752, 2024.

[7] H. Li, W. Deng, Q. Zhu, Q. Guan, and J. Luo, "Local–global context-aware generative dual-region adversarial networks for remote sensing scene image super-resolution," *IEEE Trans. Geosci. Remote Sens.*, vol. 62, 2024, Art. no. 5402114.

[8] Y. Wu, Z. Li, B. Zhao, Y. Song, and B. Zhang, "Transfer learning of spatial features from high-resolution RGB images for large-scale and robust hyperspectral remote sensing target detection," *IEEE Trans. Geosci. Remote Sens.*, vol. 62, 2024, Art. no. 5505732.

[9] R. An, X. Zhang, M. Sun, and G. Wang, "GC-YOLOv9: Innovative smart city traffic monitoring solution," *Alexandria Eng. J.*, vol. 106, pp. 277–287, Nov. 2024.

[10] B. Qian, N. Al Said, and B. Dong, "New technologies for UAV navigation with real-time pattern recognition," *Earth Syst. Sci. Data*, vol. 15, no. 3, Mar. 2024, Art. no. 102480.

[11] P. Wang, B. Bayram, and E. Sertel, "A comprehensive review on deep learning based remote sensing image super-resolution methods," *Earth-Sci. Rev.*, vol. 232, Sep. 2022, Art. no. 104110.

[12] H. Fan, Y. Chen, Y. Guo, H. Zhang, and G. Kuang, "Hyperspectral image restoration using low-rank tensor recovery," *IEEE J. Sel. Topics Appl. Earth Observ. Remote Sens.*, vol. 10, no. 10, pp. 4589–4604, Oct. 2017.

[13] S. Lei, Z. Shi, and W. Mo, "Transformer-based multistage enhancement for remote sensing image super-resolution," *IEEE Trans. Geosci. Remote Sens.*, vol. 60, pp. 1–11, 2021.

[14] C. Ma, J. Zhu, Y. Li, J. Li, Y. Jiang, and X. Li, "Single image super resolution via wavelet transform fusion and SRFeat network," *J. Ambient Intell. Humanized Comput.*, vol. 13, no. 11, pp. 5023–5031, Nov. 2022.

[15] J. Zhang, J. Lei, W. Xie, Z. Fang, Y. Li, and Q. Du, "SuperYOLO: Super resolution assisted object detection in multimodal remote sensing imagery," *IEEE Trans. Geosci. Remote Sens.*, vol. 61, 2023, Art. no. 5605415.

[16] M. Sdraka et al., "Deep learning for downscaling remote sensing images: Fusion and super-resolution," *IEEE Geosci. Remote Sens. Mag.*, vol. 10, no. 3, pp. 202–255, Sep. 2022.

[17] Q. Song, R. Xiong, D. Liu, Z. Xiong, F. Wu, and W. Gao, "Fast image super-resolution via local adaptive gradient field sharpening transform," *IEEE Trans. Image Process.*, vol. 27, no. 4, pp. 1966–1980, Apr. 2018.

[18] Y. Xiao, Q. Yuan, K. Jiang, J. He, Y. Wang, and L. Zhang, "From degrade to upgrade: Learning a self-supervised degradation guided adaptive network for blind remote sensing image super-resolution," *Inf. Fusion*, vol. 96, pp. 297–311, Aug. 2023.

[19] Y. Wang, Z. Shao, T. Lu, C. Wu, and J. Wang, "Remote sensing image super-resolution via multiscale enhancement network," *IEEE Geosci. Remote Sens. Lett.*, vol. 20, pp. 1–5, 2023.

[20] W. Dong, L. Zhang, G. Shi, and X. Wu, "Image deblurring and super-resolution by adaptive sparse domain selection and adaptive regularization," *IEEE Trans. Image Process.*, vol. 20, no. 7, pp. 1838–1857, Jul. 2011.

[21] P. Purkait, N. R. Pal, and B. Chanda, "A fuzzy-rule-based approach for single frame super resolution," *IEEE Trans. Image Process.*, vol. 23, no. 5, pp. 2277–2290, May 2014.

[22] Y. Zhang, J. Liu, W. Yang, and Z. Guo, "Image super-resolution based on structure-modulated sparse representation," *IEEE Trans. Image Process.*, vol. 24, no. 9, pp. 2797–2810, Sep. 2015.

[23] C. Dong, C. C. Loy, K. He, and X. Tang, "Image super-resolution using deep convolutional networks," *IEEE Trans. Pattern Anal. Mach. Intell.*, vol. 38, no. 2, pp. 295–307, Feb. 2016.

[24] C. Dong, C. C. Loy, and X. Tang, "Accelerating the super-resolution convolutional neural network," in *Proc. Eur. Conf. Comput. Vis.*, 2016, pp. 295–307.

[25] K. Zhang, J. Liang, L. Van Gool, and R. Timofte, "Designing a practical degradation model for deep blind image super-resolution," in *Proc. IEEE/CVF Int. Conf. Comput. Vis. (ICCV)*, Oct. 2021, pp. 4791–4800.

[26] M. Fritsche, S. Gu, and R. Timofte, "Frequency separation for real-world super-resolution," in *Proc. IEEE/CVF Int. Conf. Comput. Vis. Workshop (ICCVW)*, Oct. 2019, pp. 3599–3608.

Authorized licensed use limited to: Southwest Minzu University. Downloaded on April 18,2025 at 01:24:17 UTC from IEEE Xplore. Restrictions apply.

[27] X. Wang et al., "ESRGAN: Enhanced super-resolution generative adversarial networks," in *Proc. Comput. Vis.-ECCV Workshops*, Aug. 2018, pp. 63–79.

[28] S. Liu, S. Liu, S. Zhang, B. Li, W. Hu, and Y.-D. Zhang, "SSAU-net: A spectral–spatial attention-based U-net for hyperspectral image fusion," *IEEE Trans. Geosci. Remote Sens.*, vol. 60, 2022, Art. no. 5542116.

[29] R. Dian, S. Li, and X. Kang, "Regularizing hyperspectral and multispectral image fusion by CNN denoiser," *IEEE Trans. Neural Netw. Learn. Syst.*, vol. 32, no. 3, pp. 1124–1135, Mar. 2021.

[30] J. Li, K. Zheng, J. Yao, L. Gao, and D. Hong, "Deep unsupervised blind hyperspectral and multispectral data fusion," *IEEE Geosci. Remote Sens. Lett.*, vol. 19, pp. 1–5, 2022.

[31] J. Li, K. Zheng, Z. Li, L. Gao, and X. Jia, "X-shaped interactive autoencoders with cross-modality mutual learning for unsupervised hyperspectral image super-resolution," *IEEE Trans. Geosci. Remote Sens.*, vol. 61, 2023, Art. no. 5518317.

[32] S.-Q. Deng, L.-J. Deng, X. Wu, R. Ran, D. Hong, and G. Vivone, "PSRT: Pyramid shuffle-and-reshuffle transformer for multispectral and hyperspectral image fusion," *IEEE Trans. Geosci. Remote Sens.*, vol. 61, 2023, Art. no. 5503715.

[33] J. Li, K. Zheng, W. Liu, Z. Li, H. Yu, and L. Ni, "Model-guided coarse-to-fine fusion network for unsupervised hyperspectral image super-resolution," *IEEE Geosci. Remote Sens. Lett.*, vol. 20, pp. 1–5, 2023.

[34] J. Li, K. Zheng, L. Gao, Z. Han, Z. Li, and J. Chanussot, "Enhanced deep image prior for unsupervised hyperspectral image super-resolution," *IEEE Trans. Geosci. Remote Sens.*, vol. 63, 2025, Art. no. 5504218.

[35] J. Li, K. Zheng, L. Gao, L. Ni, M. Huang, and J. Chanussot, "Model-informed multistage unsupervised network for hyperspectral image super-resolution," *IEEE Trans. Geosci. Remote Sens.*, vol. 62, 2024, Art. no. 5516117.

[36] A. Esmaeili, K. Behdin, M. A. Fakharian, and F. Marvasti, "Transductive multi-label learning from missing data using smoothed rank function," *Pattern Anal. Appl.*, vol. 23, no. 3, pp. 1225–1233, Aug. 2020.

[37] Z. Hu, F. Nie, R. Wang, and X. Li, "Low rank regularization: A review," *Neural Netw.*, vol. 136, pp. 218–232, Apr. 2021.

[38] Y. Luo, X. Zhao, Z. Li, M. K. Ng, and D. Meng, "Low-rank tensor function representation for multi-dimensional data recovery," *IEEE Trans. Pattern Anal. Mach. Intell.*, vol. 46, no. 5, pp. 1225–1233, May 2024.

[39] X.-L. Zhao, J.-H. Yang, T.-H. Ma, T.-X. Jiang, M. K. Ng, and T.-Z. Huang, "Tensor completion via complementary global, local, and nonlocal priors," *IEEE Trans. Image Process.*, vol. 31, pp. 984–999, 2022.

[40] B.-Z. Li, X.-L. Zhao, T.-Y. Ji, X.-J. Zhang, and T.-Z. Huang, "Nonlinear transform induced tensor nuclear norm for tensor completion," *J. Sci. Comput.*, vol. 92, no. 3, pp. 1–30, Sep. 2022.

[41] Z.-C. Wu, T.-Z. Huang, L.-J. Deng, J. Huang, J. Chanussot, and G. Vivone, "LRTCFPan: Low-rank tensor completion based framework for pansharpening," *IEEE Trans. Image Process.*, vol. 32, pp. 1640–1655, 2023.

[42] R. K. Halder, M. N. Uddin, M. A. Uddin, S. Aryal, and A. Khraisat, "Enhancing K-nearest neighbor algorithm: A comprehensive review and performance analysis of modifications," *J. Big Data*, vol. 11, no. 1, p. 113, Aug. 2024.

[43] R. Fernandez-Beltran, P. Latorre-Carmona, and F. Pla, "Single-frame super-resolution in remote sensing: A practical overview," *Int. J. Remote Sens.*, vol. 38, no. 1, pp. 314–354, Jan. 2017.

[44] X. Pu and F. Xu, "Low-rank adaption on transformer-based oriented object detector for satellite onboard processing of remote sensing images," *IEEE Trans. Geosci. Remote Sens.*, vol. 63, 2025, Art. no. 5202213.

[45] Y.-R. Fan, T.-Z. Huang, J. Liu, and X.-L. Zhao, "Compressive sensing via nonlocal smoothed rank function," *PLoS ONE*, vol. 11, no. 9, Sep. 2016, Art. no. e0162041.

[46] L.-J. Deng, M. Feng, and X.-C. Tai, "The fusion of panchromatic and multispectral remote sensing images via tensor-based sparse modeling and hyper-Laplacian prior," *Inf. Fusion*, vol. 52, pp. 76–89, Dec. 2019.

[47] Y. Zhong, K. Liu, S. Gao, and X. Luo, "Alternating-direction-method of multipliers-based adaptive nonnegative latent factor analysis," *IEEE Trans. Emerg. Topics Comput. Intell.*, vol. 8, no. 5, pp. 3544–3558, Oct. 2024.

[48] H. Zhang, X.-L. Zhao, T.-X. Jiang, M. K. Ng, and T.-Z. Huang, "Multiscale feature tensor train rank minimization for multidimensional image recovery," *IEEE Trans. Cybern.*, vol. 52, no. 12, pp. 13395–13410, Dec. 2022.

[49] Y. Zhu, P. Zhou, Z. Zhang, Y. Wang, and X. Zhang, "Optimization of antenna rotation speed and super-resolution imaging based on split Bregman algorithm for circular scan ISAR systems," in *Proc. IEEE Int. Geosci. Remote Sens. Symp. (IGARSS)*, Brussels, Belgium, Jul. 2021, pp. 5083–5086.

[50] I. Bakurov, M. Buzzelli, R. Schettini, M. Castelli, and L. Vanneschi, "Structural similarity index (SSIM) revisited: A data-driven approach," *Expert Syst. Appl.*, vol. 189, Mar. 2022, Art. no. 116087.

[51] Y. Luo, X. Zhao, T. Jiang, Y. Chang, M. K. Ng, and C. Li, "Self-supervised nonlinear transform-based tensor nuclear norm for multi-dimensional image recovery," *IEEE Trans. Image Process.*, vol. 31, pp. 3793–3808, 2022.

Jiaqing Miao received the B.S. degree in mathematics from Northeast Petroleum University, Daqing, China, in 2005, the M.S. degree from the School of Mathematical, Northeastern University, Shenyang, China, in 2008, and the Ph.D. degree from the School of Mathematical Sciences, University of Electronic Science and Technology of China, Chengdu, China, in 2020.

He was a Visiting Scholar with the Department of Geophysical Engineering, Montana Technological University, Butte, MT, USA, from 2016 to 2018. He is currently an Associate Professor with the School of Computer Science and Technology, Southwest Minzu University, Chengdu. His research interests include digital image processing and applications to medical imaging and remote sensing, including image segmentation, image inpainting, image clustering, compressed sensing, and remotely sensed image reconstruction.

Xiaobing Zhou received the B.S. degree in physics from Hunan Normal University, Changsha, China, in 1986, the M.S. degree in theoretical physics from Sichuan University, Chengdu, China, in 1989, and the Ph.D. degree in geophysics from the University of Alaska, Fairbanks, AK, USA, in 2002, with a specialization in remote sensing.

He was with the Southwestern Institute of Physics, Chengdu, as a Research Assistant Professor from 1989 to 1997 and a Research Associate Professor from 1995 to 1997. He was a Visiting Scientist with the University of California at San Diego, La Jolla, CA, USA, in 1997. He was a Visiting Scientist with the Institute of Geophysics, University of Alaska, in 1998. He was a Research Assistant Professor with New Mexico Tech, Socorro, NM, USA, from 2002 to 2005. Since 2005, he has been an Assistant Professor in geophysical engineering with the Department of Geophysical Engineering, Montana Technological University, Butte, MT, USA, where he has been an Associate Professor since 2009 and a Full Professor since 2014. His research interests include remote sensing theories, algorithm development and instrumentation (optical remote sensing and imaging radar), image data collection and processing, and applications in earth and environmental sciences, including geophysical exploration.

Guibing Li received the B.S. degree in computer and application from the University of Electronic Science and Technology of China, Chengdu, China, in 2001, and the M.S. degree from the School of Computer Science and Engineering, University of Electronic Science and Technology of China, in 2003. He is currently pursuing the Ph.D. degree with the School of Electrical Engineering, Southwest Jiaotong University, Chengdu.

He is currently a Lecturer with the School of Computer Science and Technology, Southwest Minzu University, Chengdu. His research interests include digital image processing and applications to medical imaging and remote sensing, including image segmentation, image inpainting, image clustering, compressed sensing, and remotely sensed image reconstruction.

Authorized licensed use limited to: Southwest Minzu University. Downloaded on April 18,2025 at 01:24:17 UTC from IEEE Xplore. Restrictions apply.

Gaoping Li received the M.Sc. degree in application mathematics from Chongqing University, Chongqing, China, in 2005.

He is currently a Professor with the School of Mathematics, Southwest Minzu University, Chengdu, China. His recent research interests include fractal theory and its applications in image processing and compressed sensing.

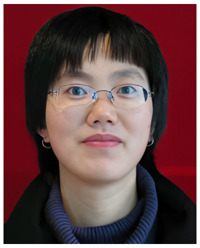

Li Zeng received the B.S. degree in mathematics from Southwest China Normal University, Chongqing, China, in 2001, and the M.S. degree from the School of Applied Mathematics, University of Electronic Science and Technology of China, Chengdu, China, in 2006.

She is currently an Associate Professor with the School of Mathematics, Southwest Minzu University, Chengdu. Her research interests include numerical computation, Perron root computation, eigenvalues of large matrices, and solutions of eigenvectors.

Xiaoguang Liu received the Ph.D. degree in mathematics from Shaanxi Normal University, Xi'an, China, in 2014.

Since 2017, he has been a Post-Doctoral Fellow at the School of Computer Science and Engineering, University of Electronic Science and Technology of China (UESTC), Chengdu, China. He is currently a Lecturer with the School of Mathematics, Southwest Minzu University, Chengdu. His recent research interests include cryptography and network security.

Ying Tan received the M.S. and Ph.D. degrees in mechanical engineering from Sichuan University, Chengdu, China, in 2002 and 2008, respectively.

He is currently a Professor with Southwest Minzu University, Chengdu, where he is also the Director of the Key Laboratory of Computer Systems, State Ethnic Affairs Commission. His research interests include artificial intelligence and functional neuroimaging.

Authorized licensed use limited to: Southwest Minzu University. Downloaded on April 18,2025 at 01:24:17 UTC from IEEE Xplore. Restrictions apply.